Wave-Current Interaction in an Oceanic Circulation Model with a Vortex-Force Formalism: Application to the Surf Zone

Yusuke Uchiyama[a,*], James C. McWilliams[a], Alexander F. Shchepetkin[a]

[a]*Institute of Geophysics and Planetary Physics, University of California, Los Angeles, CA, U.S.A.*

Abstract

A vortex-force formalism for the interaction of surface gravity waves and currents is implemented in a three-dimensional (3D), terrain-following, hydrostatic, oceanic circulation model (Regional Oceanic Modeling System: ROMS; Shchepetkin and McWilliams, 2005). Eulerian wave-averaged current equations for mass, momentum, and tracers are included in ROMS based on an asymptotic theory by McWilliams et al. (2004) plus non-conservative wave effects due to wave breaking, associated surface roller waves, bottom streaming, and wave-enhanced vertical mixing and bottom drag especially for coastal and nearshore applications. The currents are coupled with a spectrum-peak WKB wave-refraction model that includes the effect of currents on waves, or, alternatively, a spectrum-resolving wave model (*e.g.*, SWAN) is used. The coupled system is applied to the nearshore surf zone during the DUCK94 field measurement campaign. Model results are compared to the observations and effects of parameter choices are investigated with emphasis on simulating and interpreting the vertical profiles for alongshore and cross-shore currents. The model is further compared to another ROMS-based 3D coupled model by Warner et al. (2008) with depth-dependent radiation stresses on a plane beach. In both tests the present model manifests an onshore surface flow and compensating offshore near-bed undertow near the shoreline and around the breaking point. In contrast, the radiation-stress prescription yields significantly weaker vertical shear. The currents' cross-shore and vertical structure is significantly shaped by the wave effects of near-surface breaker acceleration, vertical component of vortex force, and wave-enhanced pressure force and bottom drag.

Key words: wave-current interaction, vortex force, ROMS, littoral current

1. Introduction

The effects of wind-driven (primary) surface gravity waves on oceanic currents and turbulence (hereafter called WEC) have been recognized to play a crucial role for scientific and engineering applications, ranging from wave-induced upper-ocean mixing and current profiles to littoral flow, sea level, and sediment transport relevant to beach management and navigation. An essential feature of most theoretical approaches to WEC is averaging over the fast oscillations of the primary wind-driven waves, with seminal papers by Longuet-Higgins (1970), Hasselmann (1971), Craik and Leibovich (1976), and Garrett (1976). Wave averaging is also necessary for feasible computations of realistic circulations with WEC.

*Corresponding author. Address: 3845 Slichter Hall, CA 90095-1565, U.S.A. Phone: +1-310-825-5402, Fax: +1-310-206-3051.

Email addresses: uchiyama@atmos.ucla.edu (Yusuke Uchiyama), jcm@atmos.ucla.edu (James C. McWilliams), alex@atmos.ucla.edu (Alexander F. Shchepetkin)

A central arena for WEC is the surf zone where breaking waves accelerate alongshore and rip currents. The interplay between waves and currents has been investigated mostly in one- or two-dimensional, depth-averaged models with fast-wave averaging (recent studies by Ruessink et al., 2001; Yu and Slinn, 2003; Özkan-Haller and Li, 2003; Reniers et al., 2004a; Uchiyama et al., 2009). Alternatively, a phase-resolving horizontal two-dimensional (2D) approach (*e.g.,* Chen et al., 1999; Terrile et al., 2008) can depict wave-current interaction processes, albeit at a prohibitive computational cost for longer-term, larger-scale current evolution.

Several wave-averaged 3D circulation models have been created during the last decade. In Walstra et al. (2000) and Lesser et al. (2004), the Delft3D-flow code includes WEC by loosely adapting a set of generalized Lagrangian mean (GLM) equations by Groeneweg (1999), adapted from Andrews and McIntyre (1978a,b). The model prognostic field is Lagrangian mean velocity $\mathbf{u}^{\ell}$ and the wave-induced forcing in the flow model is represented by the depth-averaged radiation-stress gradient (*e.g.,* Longuet-Higgins and Stewart, 1962; Hasselmann, 1971; Phillips, 1977), although in practice it is expressed in terms of breaking and frictional dissipation terms provided by a wave model in accordance with Dingemans et al. (1987) and imposed in the flow model as surface and bottom stresses. A simple, geostrophic 3D GLM ocean model was proposed by Perrie et al. (2003) where Stokes-Coriolis force (Hasselmann, 1971) and a surface-intensified acceleration due to wave dissipation are taken into account as WEC. These models neglected the conservative vortex force (VF) and quasi-static set-down (*i.e.,* equivalent to a pressure contribution in the Longuet-Higgins and Stewart (1962) radiation stress). Another branch of engineering-oriented 3D modeling with WEC is by Xie et al. (2001), following Lewis (1997). It applies the depth-averaged radiation-stress gradient as a depth-uniform body force in the Princeton Ocean Model (POM; Blumberg and Mellor (1987)). Later, a depth-dependent form of horizontal radiation stress gradient terms was proposed by Xia et al. (2004) in a theoretically *ad hoc* way. Warner et al. (2008) (W08) employs a GLM-like vertical mapping approach with a depth-dependent radiation-stress formalism proposed by Mellor (2003, 2005) in the Regional Oceanic Modeling System (ROMS) code. It is recognized (Ardhuin et al., 2008a) that accurate implementation of this formalism (also the "alternative" GLM equations in Andrews and McIntyre (1978a)) requires knowledge of the wave kinematics to higher order in parameters that define the large-scale evolution of the wave field, such as the bottom slope; this impracticality is addressed in Mellor (2008), but it does not yet seem to have been conveyed into the W08 code. In these 3D models the WEC are represented as the radiation stress gradient. Based on the Helmholtz decomposition of the advection terms in the equations of motion, the VF representation comes from the identity, $\mathbf{u}\cdot\nabla\mathbf{u} = \nabla|\mathbf{u}|^2/2 + (\nabla\times\mathbf{u})\times\mathbf{u}$, while the radiation-stress representation arises from the Reynolds decomposition, $\mathbf{u}\cdot\nabla\mathbf{u} = \nabla\cdot(\mathbf{uu}) + \mathbf{u}(\nabla\cdot\mathbf{u})$, together with incompressibility $\nabla\cdot\mathbf{u} = 0$, where $\mathbf{u}$ is the Eulerian velocity. The primary advantage of the wave-averaged VF formalism is its explicit inclusion of a type of wave-current interaction that few if any available wave models properly incorporate to allow its complete expression in the radiation stress (*e.g.,* Lane et al., 2007). A conspicuous demonstration of the utility of a VF representation is Langmuir circulations in the upper ocean (Craik and Leibovich, 1976; Leibovich, 1980; McWilliams et al., 1997). The GLM approach with a VF formalism is taken in Ardhuin et al. (2008b) and advocated as appropriate for a wide range of oceanic applications. This formulation is applied to vertical one-dimensional modeling of the ocean mixed layer by Rascle et al. (2006, 2009) and tested in a nearshore 2D (cross-shore/vertical) (Rascle, 2007). Instead, we utilize an Eulerian reference frame for the wave averaging (*e.g.,* McWilliams and Restrepo, 1999; McWilliams et al., 2004; Lane et al., 2007), primarily for more direct comparability to most measurements and compatibility with existing circulation models. Within asymptotic approximations the two approaches are equivalently valid as long as the Lagrangian and Eulerian mean velocities are related by $\mathbf{u}^{\ell} = \mathbf{u} + \mathbf{u}^{St}$, where $\mathbf{u}^{St}$ is the 3D Stokes drift velocity. When the model prognostic variable is $\mathbf{u}^{\ell}$, care must be taken to retrieve $\mathbf{u}$ to estimate horizontal and vertical mixing, bed shear stress, and boundary conditions for realistic applications.

For littoral currents in the surf zone, Longuet-Higgins (1973) and Dingemans et al. (1987) show that conservative and non-conservative contributions in WEC are separable within the radiation stress divergence when a geometric optics (WKB, ray theory) approximation is applied to the wave field; the VF is contained within the radiation stress divergence, but they argued that it is negligible in a surface zone when the breaking-induced acceleration dominates. However, this assumption has been partially falsified in several models with a VF formalism: barotropic models (Smith, 2006; Uchiyama et al., 2009), a quasi-3D model (Shi et al., 2006), and 3D models (Newberger and Allen, 2007a,b, called "nearshore POM" and designated by NA07, and Delft3D-flow). Multiple aspects of WEC are expected to be important for surf zone currents. In addition to the conservative effects of VF, Bernoulli head, and quasi-static pressure response, there are important non-conservative effects due to depth-induced breaking (and white capping) near the surface and frictional wave dissipation near the bottom. For 3D configurations the last two components should be applied at appropriate depths, near the surface for the former and right above the wave bottom boundary layer for the latter.

In this paper we develop and test a 3D oceanic circulation model (extending ROMS; Shchepetkin and McWilliams 2005) with dynamically consistent wave-current interactions suitable to a wide range of nearshore, coastal, and open-ocean applications. We base the model on the Eulerian-averaged, multi-scale, wave-current asymptotic theory derived in McWilliams et al. (2004) (MRL04). It uses a VF formalism that cleanly separates conservative and non-conservative WEC mechanisms, unlike the radiation-stress formalism. The conservative part of WEC comprises the VF (Leibovich, 1980), the Stokes-Coriolis force (Hasselmann, 1971), Bernoulli head, and a quasi-static pressure response known as wave-setup/down. Non-conservative WEC are included as a surface-concentrated 3D acceleration and wave-enhanced vertical mixing due to depth-induced wave breaking and associated surface rollers; a bottom-confined bottom streaming stress (*e.g.,* Longuet-Higgins, 1953) caused by near-bed wave drag; and a wave-enhanced current bed shear stress (*e.g.,* Soulsby, 1995). The wave-induced vertical mixing is represented as an extension of the KPP model (Large et al., 1994), a non-local vertical mixing parameterization. The governing current and wave equations are presented in Sec. 2, and the WEC implementation in ROMS is detailed in Sec. 3 with particular attention to non-conservative wave effects adapted from previous parameterizations. Section 4 describes the application to the surf zone during the DUCK94 experiment. In Sec. 5 a comparison to another ROMS-based 3D wave-current model by W08 and Haas and Warner (2009) (HW09) based on a radiation-stress formalism is made for an idealized plane beach, using an identical wave field from SWAN (Booij et al., 1999). Section 6 provides a summary and an outlook for future applications of the model.

2. Governing Equations

The WEC model formulation is built on a sequence of previous developments. McWilliams et al. (2004) (MRL04) derives a multi-scale asymptotic model for the phase-averaged, conservative dynamical effects of surface gravity waves on currents and infragravity waves with longer space and time scales. MRL04 extends earlier derivations that feature the central WEC role of VF (Craik and Leibovich, 1976; Garrett, 1976; McWilliams et al., 1997; McWilliams and Restrepo, 1999), and this approach is set in the context of the larger literature on wave-current interaction in Lane et al. (2007) (LRM07). Uchiyama and McWilliams (2008) presents a barotropic ROMS model for the effects of primary wind waves on infragravity waves, while Uchiyama et al. (2009) presents a vertically-averaged (barotropic) ROMS model for surf zone shear instability with WEC. In this and the next section we describe the governing equations and ROMS implementation for 3D WEC and an accompanying surface wave model with effects of currents on the waves (hereafter called CEW).

2.1. Wave-Averaged Currents

ROMS is a hydrostatic, incompressible (Boussinesq), free-surface model with non-conservative forcing, diffusion, and bottom drag. It makes a baroclinic-barotropic mode split, with explicit fast time-stepping and subsequent conservative averaging of barotropic variables. All present elements in ROMS are retained, but new terms are added to incorporate WEC[1]. The ROMS formulation is non-asymptotic in the sense that some additional non-wave terms, beyond the minimum required for asymptotic consistency as defined in MRL04, are included for completeness (*e.g.*, the time-derivative of surface elevation in the kinematic boundary condition and depth-integrated mass balance), along with additional non-conservative wave effects (*e.g.*, breaker acceleration).

We first write the model equations in Cartesian (x, y, z, t) coordinates. The notation is slightly different from MRL04, and the quantities are dimensional. We combine the infragravity wave and current dynamics, which were asymptotically separated in MRL04. The momentum balance is written in terms of a dynamic pressure ϕ (normalized by mean density ρ_0) and sea level ζ after subtracting the wave-averaged quasi-static components $\hat{\phi}$ and $\hat{\zeta}$ (*n.b.*, MRL04, Secs. 6 & 9.2-3 and LRM07, eqs. (3.8)-(3.10)) that occur even without currents. All wave quantities are referenced to the local wave-averaged sea level, $z = \zeta + \hat{\zeta}$, rather than the mean sea level, $z = 0$. The vertical coordinate range is $-h(\mathbf{x}) \le z \le \zeta + \hat{\zeta}$. The equations make the particular gauge choice for the decomposition between VF ($\mathbf{J}$, K) and Bernoulli head $\mathcal{K}$ described in MRL04, Sec. 9.6. The new WEC terms for ROMS are written on the right side of the equations below. Boldface vectors are horizontal only, and 3D vectors are designated by (**horizontal**, vertical).

$$
\begin{aligned}
\frac{\partial \mathbf{u}}{\partial t} + (\mathbf{u}\cdot\boldsymbol{\nabla}_\perp)\mathbf{u} + w\frac{\partial \mathbf{u}}{\partial z} + f\hat{\mathbf{z}}\times\mathbf{u} + \boldsymbol{\nabla}_\perp\phi - \mathbf{F} &= -\boldsymbol{\nabla}_\perp\mathcal{K} + \mathbf{J} + \mathbf{F}^w \\
\frac{\partial \phi}{\partial z} + \frac{g\rho}{\rho_0} &= -\frac{\partial \mathcal{K}}{\partial z} + K \\
\boldsymbol{\nabla}_\perp\cdot\mathbf{u} + \frac{\partial w}{\partial z} &= 0 \\
\frac{\partial c}{\partial t} + (\mathbf{u}\cdot\boldsymbol{\nabla}_\perp)c + w\frac{\partial c}{\partial z} - C &= -(\mathbf{u}^{St}\cdot\boldsymbol{\nabla}_\perp)c - w^{St}\frac{\partial c}{\partial z} + \frac{1}{2}\frac{\partial}{\partial z}\left[\mathcal{E}\frac{\partial c}{\partial z}\right] .
\end{aligned}
\tag{1}
$$

$\mathbf{F}$ is the non-wave non-conservative forces, $\mathbf{F}^w$ is the wave-induced non-conservative forces, c is any material tracer concentration (*e.g.*, T and S), and C is the non-conservative tracer forcing, where $\boldsymbol{\nabla}_\perp$ is the horizontal differential operator. The system (1) is completed with the equation of state.

The 3D Stokes velocity ($\mathbf{u}^{St}$, w^{St}) is non-divergent and defined for a monochromatic wave field by

$$
\begin{aligned}
\mathbf{u}^{St} &= \frac{A^2\sigma}{2\sinh^2[\mathcal{H}]}\cosh[2\mathcal{Z}]\mathbf{k} \\
w^{St}(z) &= -\boldsymbol{\nabla}_\perp\cdot\int_{-h}^{z}\mathbf{u}^{St}\,dz' .
\end{aligned}
\tag{2}
$$

$h(\mathbf{x})$ is the resting depth of the ocean.; A is the wave amplitude; $\mathbf{k}$ is its wavenumber vector and k is its magnitude;

[1]The recent generalization to a non-hydrostatic ROMS model (Kanarska et al., 2007) will include the same wave-averaged effects discussed here. Additional terms are added to the momentum equations: non-WEC terms for vertical acceleration and for horizontal Coriolis frequency f^y and WEC terms for Stokes-Coriolis force with f^y and for VF with full horizontal vorticity

$$\sigma = \sqrt{gk\tanh[\mathcal{H}]} \tag{3}$$

is its intrinsic frequency; and normalized vertical lengths are

$$\mathcal{H} = k(h+\zeta+\hat{\zeta}) \equiv kD; \quad \text{and} \quad \mathcal{Z} = k(z+h)\,, \tag{4}$$

where $D = h+\zeta+\hat{\zeta}$ is the wave-averaged thickness of the water column. The horizontal and vertical VF (inclusive of the Stokes-Coriolis term) and Bernoulli head (after removing quasi-static terms) are

$$\begin{aligned}
\mathbf{J} &= -\hat{\mathbf{z}}\times\mathbf{u}^{St}\left((\hat{\mathbf{z}}\cdot\boldsymbol{\nabla}_\perp\times\mathbf{u}) + f\right) - w^{St}\frac{\partial\mathbf{u}}{\partial z} \\
K &= \mathbf{u}^{St}.\frac{\partial\mathbf{u}}{\partial z} \\
\mathcal{K} &= \frac{1}{4}\frac{\sigma A^2}{k\sinh^2[\mathcal{H}]}\int_{-h}^{z}\frac{\partial^2\mathcal{V}}{\partial z'^2}\,\sinh[2k(z-z')]\,dz'\,,
\end{aligned} \tag{5}$$

with $\mathcal{V} = \mathbf{k}\cdot\mathbf{u}$. The wave-induced tracer diffusivity is defined by

$$\mathcal{E} = \frac{1}{2}\frac{\partial}{\partial t}\left(\frac{A\sinh[\mathcal{Z}]}{\sinh[\mathcal{H}]}\right)^2\,. \tag{6}$$

The quasi-static sea-level component is defined by

$$\hat{\zeta} = -\frac{p_{atm}}{g\rho_0} - \frac{A^2k}{2\sinh[2\mathcal{H}]}\,. \tag{7}$$

It contains both an inverse-barometric response to changes in atmospheric pressure p_{atm} and a wave-averaged set-up/set-down.

With a multi-component wave field, A^2 is replaced in (2)-(7) by the sea-level spectrum $G(\theta,\sigma)$ with integration over wavenumber-vector angle θ and frequency σ. This implies a superposition of the WEC contributions from different components, consistent with the asymptotic theoretical assumption of small wave slope Ak.

2.2. Boundary Conditions

The boundary conditions for ROMS include the usual stress and heat and material flux conditions plus the following kinematic and pressure continuity conditions, again with the additional WEC terms on the right side:

$$\begin{aligned}
w\Big|_{-h} + \mathbf{u}\Big|_{-h}\cdot\boldsymbol{\nabla}_\perp h &= 0 \\
w\Big|_{\zeta+\hat{\zeta}} - \frac{\partial\zeta}{\partial t} - (\mathbf{u}\Big|_{\zeta+\hat{\zeta}}\cdot\boldsymbol{\nabla}_\perp)\zeta &= \boldsymbol{\nabla}_\perp\cdot\overline{\mathbf{U}}^{St} + \frac{\partial\hat{\zeta}}{\partial t} + (\mathbf{u}\Big|_{\zeta+\hat{\zeta}}\cdot\boldsymbol{\nabla}_\perp)\hat{\zeta} \\
g\zeta - \phi\Big|_{\zeta+\hat{\zeta}} &= \mathcal{P}\,,
\end{aligned} \tag{8}$$

with

$$\mathcal{P} = \frac{A^2}{2\sigma}\Big\{\frac{\tanh[\mathcal{H}]}{\sinh[2\mathcal{H}]}\left(-\frac{\partial\mathcal{V}}{\partial z}\Big|_{\zeta+\hat\zeta} + \cosh[2\mathcal{H}]\frac{\partial\mathcal{V}}{\partial z}\Big|_{-h} + \int_{-h}^{\zeta+\hat\zeta}\frac{\partial^2\mathcal{V}}{\partial z'^2}\cosh[2kz']\,dz'\right) - 2k\tanh[\mathcal{H}]\mathcal{V}\Big|_{\zeta+\hat\zeta}\Big\}. \tag{9}$$

In MRL04, Sec. 9.3, there are additional quasi-static components in $\mathcal{P}$ of higher asymptotic order in the wave slope Ak, but, unlike in $\hat\zeta$ in (8), they have no dynamical coupling with the currents in (1) and (8). So, without a specific motivation for examining the various deleted quasi-static terms, they are not presently included in ROMS, although they could easily be added as a diagnostic.

2.3. Barotropic Mode

The barotropic mode is derived from (1) as a vertical integral of the continuity equation and a vertical average of the horizontal momentum equation. With the WEC terms kept on the right side, the result is

$$\begin{aligned}\frac{\partial\zeta}{\partial t} + \boldsymbol{\nabla}_\perp\cdot\overline{\mathbf{U}} &= -\frac{\partial\hat\zeta}{\partial t} - \boldsymbol{\nabla}_\perp\cdot\overline{\mathbf{U}}^{St}\\ \frac{\partial\overline{\mathbf{u}}}{\partial t} + \frac{1}{D}(\boldsymbol{\nabla}_\perp\cdot\overline{\mathbf{U}})\left(\mathbf{u}\Big|_{\zeta+\hat\zeta} - \frac{\overline{\mathbf{U}}}{D}\right) + \ldots &= -\frac{1}{D}(\boldsymbol{\nabla}_\perp\cdot\overline{\mathbf{U}}^{St})\left(\mathbf{u}\Big|_{\zeta+\hat\zeta} - \frac{\overline{\mathbf{U}}}{D}\right)\\ &\quad + \frac{1}{D}\int_{-h}^{\zeta+\hat\zeta}[\mathbf{J} - \boldsymbol{\nabla}_\perp\mathcal{K}]\,dz + \overline{\mathbf{F}}^{w}.\end{aligned} \tag{10}$$

The dots in the barotropic momentum equation indicate contributions from all the left-side terms in the horizontal momentum equation in (1) other than the acceleration. Here

$$\overline{\mathbf{U}} = \int_{-h}^{\zeta+\hat\zeta}\mathbf{u}\,dz \quad\text{and}\quad \overline{\mathbf{U}}^{St} = \int_{-h}^{\zeta+\hat\zeta}\mathbf{u}^{St}\,dz \tag{11}$$

are the horizontal volume transports by Eulerian and Stokes currents, respectively, and $\overline{\mathbf{u}} = \overline{\mathbf{U}}/D$ is the barotropic velocity. (Note that the depth integration and averaging violates the strict separation of non-wave and wave-averaged terms on the left and right sides of the equations above.) We can combine the barotropic continuity and momentum equations in (10) to write the latter in the form used in ROMS:

$$\frac{\partial}{\partial t}\overline{\mathbf{U}} + \ldots = -\mathbf{u}\Big|_{\zeta+\hat\zeta}\boldsymbol{\nabla}_\perp\cdot(\overline{\mathbf{U}} + \overline{\mathbf{U}}^{St}) + \int_{-h}^{\zeta+\hat\zeta}[\mathbf{J} - \boldsymbol{\nabla}_\perp\mathcal{K}]\,dz + D\overline{\mathbf{F}}^{w}. \tag{12}$$

The free-surface equation in (10) implies the volume conservation relation,

$$\frac{d}{dt}\int\int(h + \zeta + \hat\zeta)\,d\mathbf{x} = -\oint(\overline{\mathbf{U}} + \overline{\mathbf{U}}^{St})\cdot\hat{\mathbf{n}}\,ds. \tag{13}$$

Thus, mean sea level within a domain is controlled by the boundary Eulerian and Stokes fluxes.

In a barotropic ROMS model, $\mathbf{u}(\zeta + \hat\zeta) = \overline{\mathbf{U}}/D$, and the remaining right-side terms are evaluated with $\mathbf{u} = \overline{\mathbf{u}}$ in $\mathbf{J}$ from (5) and $\mathcal{K} = 0$. The associated tracer variable is also equated with its depth-averaged value, $c = \overline{c}$. The resulting model has been applied to infragravity-wave and nearshore barotropic shear-instability problems (Uchiyama and McWilliams, 2008; Uchiyama et al., 2009).

2.4. Wave Dynamics

For a monochromatic wave field, a WKB wave model with wave refraction and conservation of wave action is the following:

$$\frac{\partial \mathbf{k}}{\partial t} + \mathbf{c}_g \cdot \boldsymbol{\nabla}_\perp \mathbf{k} = -\tilde{\mathbf{k}} \cdot \boldsymbol{\nabla}_\perp \tilde{\bar{\mathbf{u}}} - \frac{k\sigma}{\sinh 2kD} \boldsymbol{\nabla}_\perp D \tag{14}$$

$$\frac{\partial \mathcal{A}}{\partial t} + \boldsymbol{\nabla}_\perp \cdot (\mathcal{A}\mathbf{c}_g) = -\frac{\epsilon^w}{\sigma}\,, \tag{15}$$

using the tilde convention to identify conjoined horizontal vectors in a dot product. The wave action is defined by $\mathcal{A} = E/\sigma$ where $E = \frac{1}{2}\rho_0 g A^2$ is the depth-integrated wave energy.

$$\sigma_{ds} = \bar{\mathbf{u}} \cdot \mathbf{k} + \sigma \tag{16}$$

is a Doppler-shifted (CEW) wave frequency, where $\bar{\mathbf{u}}$ is the depth-averaged current[2], σ is the intrinsic frequency (3), and the associated group velocity is

$$\mathbf{c_g} = \bar{\mathbf{u}} + \frac{\sigma}{2k^2}\left(1 + \frac{2kD}{\sinh 2kD}\right)\mathbf{k}\,. \tag{17}$$

ϵ^w is the depth-integrated rate of wave energy loss (or dissipation). In the present formulation we include wave dissipation due to depth-induced breaking and bottom drag, both of which must be parameterized (Sec. 3.2).

In some realistic cases, this model is applied with $\mathbf{k} = \mathbf{k}_p$ the spectrum-peak wavenumber and $A = \sqrt{2E}/g = H_{sig}/(2\sqrt{2}) = H_*/2$ the equivalent wave amplitude in terms of the wave energy E, the so-called significant wave height H_{sig}, or a wave height H_* commonly used in breaking parameterizations. The simplest extension from a monochromatic/spectrum-peak model to a multi-component model is based on superposition of components with spectrum G. For more general wave dynamics including nonlinear spectrum evolution and wind generation, a wave simulation model is used (*e.g.,* SWAN; Booij et al., 1999) to provide G and ϵ^w. One may also specify G from available observations, *e.g.,* an offshore wave buoy.

3. Implementation in ROMS

3.1. Wave-Averaged 3D Currents and Tracers

As a prelude to discretization in curvilinear coordinates, we rewrite several of the WEC relations in Sec. 2 in forms closer to those used in ROMS, adopting a flux-divergence form of the substantial derivative and defining three new variables,

[2]This CEW theory is strictly valid only for depth-uniform currents because strong vertical current shear invalidates the wave eigenmodes and dispersion relation on which the asymptotic WEC theory is based. In practice we use either the depth-average current in shallow water or an upper-ocean average over a depth $\propto k^{-1}$ in deep water for the wave model. MRL04 did not include CEW because its scaling assumptions were that current speed and sea level elevation are respectively smaller than gravity-wave propagation speed and resting depth.

$$
\begin{aligned}
\zeta^c &= \zeta + \hat{\zeta} \\
\phi^c &= \phi + \mathcal{K} \\
\left(\mathbf{u}^\ell, \omega^\ell\right) &= (\mathbf{u}, \omega) + \left(\mathbf{u}^{St}, \omega^{St}\right) ,
\end{aligned} \tag{18}
$$

where ζ^c is a composite sea level, ϕ^c absorbs the Bernoulli head, $(\mathbf{u}^\ell, \omega^\ell)$ is the wave-averaged Lagrangian velocity, and ω is the vertical velocity in the transformed coordinate system used in ROMS (see (25) *et seq.*). The 3D Primitive Equations (1) become

$$
\begin{aligned}
\frac{\partial \mathbf{u}}{\partial t} + \tilde{\boldsymbol{\nabla}}_\perp\cdot(\tilde{\mathbf{u}^\ell}\mathbf{u}) + \frac{\partial}{\partial z}\left(w^\ell \mathbf{u}\right) + f\hat{\mathbf{z}}\times\mathbf{u}^\ell + \boldsymbol{\nabla}_\perp\phi^c - \mathbf{F} &= \mathbf{u}^{\tilde{St}}\boldsymbol{\nabla}_\perp\cdot\tilde{\mathbf{u}} + \mathbf{F}^w \\
\frac{\partial \phi^c}{\partial z} + \frac{g\rho}{\rho_0} &= K \\
\boldsymbol{\nabla}_\perp\cdot\mathbf{u}^\ell + \frac{\partial w^\ell}{\partial z} &= 0 \\
\frac{\partial c}{\partial t} + \tilde{\boldsymbol{\nabla}}_\perp\cdot(\tilde{\mathbf{u}}^\ell c) + \frac{\partial}{\partial z}\left(w^\ell c\right) - C &= \frac{1}{2}\frac{\partial}{\partial z}\left[\mathcal{E}\frac{\partial c}{\partial z}\right] .
\end{aligned} \tag{19}
$$

The WEC terms are no longer confined to the right sides of these equations. The boundary conditions (8) are

$$
\begin{aligned}
w^\ell\Big|_{-h} + \mathbf{u}^\ell\Big|_{-h}\cdot\boldsymbol{\nabla}_\perp h &= 0 \\
w^\ell\Big|_{\zeta^c} - \frac{\partial \zeta^c}{\partial t} - (\mathbf{u}^\ell\Big|_{\zeta^c}\cdot\boldsymbol{\nabla}_\perp)\zeta^c &= 0 \\
g\zeta^c - \phi^c\Big|_{\zeta^c} &= \mathcal{P} + g\hat{\zeta} - \mathcal{K}\Big|_{\zeta^c} .
\end{aligned} \tag{20}
$$

The depth-integrated continuity equation in (10) is

$$
\frac{\partial \zeta^c}{\partial t} + \boldsymbol{\nabla}_\perp\cdot\overline{\mathbf{U}}^\ell = 0 , \tag{21}
$$

where $\overline{\mathbf{U}}^\ell$ is the depth integral of $\mathbf{u}^\ell$. The associated barotropic horizontal momentum equation (12) is

$$
\frac{\partial}{\partial t}\overline{\mathbf{U}} + \tilde{\boldsymbol{\nabla}}_\perp\cdot\int_{-h}^{\zeta^c}(\tilde{\mathbf{u}}^\ell\mathbf{u})\,dz = -gD\boldsymbol{\nabla}_\perp\zeta^c + \mathscr{F}' + \int_{-h}^{\zeta^c}\mathbf{R}\,dz , \tag{22}
$$

where $\mathscr{F}'$ is the baroclinic part of the full vertically-integrated pressure-gradient force,

$$
\mathscr{F}' = gD\boldsymbol{\nabla}_\perp\zeta^c - \int_{-h}^{\zeta^c}\boldsymbol{\nabla}_\perp\phi^c\,dz , \tag{23}
$$

containing the usual terms proportional to $g\rho'/\rho_0$ as well as contributions from wave effects, but excluding the barotropic free-surface gradient term. Other terms in the 3D momentum equation in (19) have been lumped into a residual horizontal vector,

$$
\mathbf{R} = -f\hat{\mathbf{z}}\times\mathbf{u}^\ell + \mathbf{F} + \mathbf{u}^{\tilde{St}}\boldsymbol{\nabla}_\perp\cdot\tilde{\mathbf{u}} + \mathbf{F}^w . \tag{24}
$$

The ROMS equations are expressed in horizontal orthogonal curvilinear and vertical surface- and terrain-following coordinates (ξ, η, s) (Shchepetkin and McWilliams, 2005, 2008). We use the composite sea-level variable ζ^c and h to define the s coordinate. m^{-1} and n^{-1} are Lamé metric coefficients, and H_z^c is the transformed grid-cell thickness. The 3D primitive equations for wave-averaged currents in ROMS are the following:

$$\frac{\partial}{\partial t}\left(\frac{H_z^c}{mn}\right) + \frac{\partial}{\partial \xi}\left(\frac{H_z^c u^\ell}{n}\right) + \frac{\partial}{\partial \eta}\left(\frac{H_z^c v^\ell}{m}\right) + \frac{\partial}{\partial s}\left(\frac{\omega_s^\ell}{mn}\right) = 0 \tag{25}$$

$$\frac{\mathscr{D}u}{\mathscr{D}t} - \hat{\mathcal{F}}^\ell v = -\frac{H_z^c}{n}\frac{\partial \phi^c}{\partial \xi}\bigg|_z + \hat{\mathcal{F}}^c v^{St} + \frac{H_z^c}{n}\left(u^{St}\frac{\partial u}{\partial \xi} + v^{St}\frac{\partial v}{\partial \xi}\right) + \frac{H_z^c}{mn}\left(\mathcal{F}^\xi + F^{w\xi}\right) \tag{26}$$

$$\frac{\mathscr{D}v}{\mathscr{D}t} + \hat{\mathcal{F}}^\ell u = -\frac{H_z^c}{m}\frac{\partial \phi^c}{\partial \eta}\bigg|_z - \hat{\mathcal{F}}^c u^{St} + \frac{H_z^c}{m}\left(u^{St}\frac{\partial u}{\partial \eta} + v^{St}\frac{\partial v}{\partial \eta}\right) + \frac{H_z^c}{mn}\left(\mathcal{F}^\eta + F^{w\eta}\right) . \tag{27}$$

$\mathscr{D}/\mathscr{D}t$ is the material derivative in conservation form in curvilinear coordinates,

$$\frac{\mathscr{D}*}{\mathscr{D}t} = \frac{\partial}{\partial t}\left(\frac{H_z^c}{mn}*\right) + \frac{\partial}{\partial \xi}\left(\frac{H_z^c u^\ell}{n}*\right) + \frac{\partial}{\partial \eta}\left(\frac{H_z^c v^\ell}{m}*\right) + \frac{\partial}{\partial s}\left(\frac{\omega_s^\ell}{mn}*\right) . \tag{28}$$

$\hat{\mathcal{F}}^\ell$ and $\hat{\mathcal{F}}^c$ are generalized Coriolis frequencies combined with the curvilinear metric terms,

$$\hat{\mathcal{F}}^\ell = H_z^c\left[\frac{f}{mn} - u^\ell \frac{\partial}{\partial \eta}\left(\frac{1}{m}\right) + v^\ell \frac{\partial}{\partial \xi}\left(\frac{1}{n}\right)\right] \tag{29}$$

$$\hat{\mathcal{F}}^c = H_z^c\left[\frac{f}{mn} - u\frac{\partial}{\partial \eta}\left(\frac{1}{m}\right) + v\frac{\partial}{\partial \xi}\left(\frac{1}{n}\right)\right] . \tag{30}$$

$\mathbf{F} = (\mathcal{F}^\xi, \mathcal{F}^\eta)$ is the non-wave body force and parameterized momentum mixing term; $\mathbf{F}^w = (F^{w\xi}, F^{w\eta})$ is the non-conservative wave terms defined later in this section. The vertical motion past s surfaces is

$$\omega_s^\ell = \left[w^\ell - \left(\frac{\partial z}{\partial t} + \mathbf{u}^\ell \cdot \boldsymbol{\nabla}_\perp z\right)\right]\Big|_s , \tag{31}$$

and the vertical mass flux is calculated as

$$W^\ell = \int_{-1}^{s}\left(\frac{\partial U^\ell}{\partial \xi} + \frac{\partial V^\ell}{\partial \eta}\right)\mathrm{d}s' - \frac{1}{mn}\cdot\frac{z+h}{\zeta+h}\cdot\frac{\partial \zeta^c}{\partial t} . \tag{32}$$

Here $U^\ell = H_z^c u^\ell/n$, $V^\ell = H_z^c v^\ell/m$, and $W^\ell = \omega_s^\ell/(mn)$ are grid-cell volume fluxes. The geopotential function is evaluated from integration of the vertical momentum equation,

$$\phi^c = g(\zeta^c - \hat{\zeta}) - (\mathcal{P} - \mathcal{K})\,|_{\zeta^c} + \int_s^0 \left[\frac{g\rho}{\rho_0} - K\right] H_z^c\, ds . \tag{33}$$

The 3D tracer equation with WEC is

$$\frac{\mathscr{D}c}{\mathscr{D}t} = C + \frac{\partial}{\partial s}\left[\frac{\mathcal{E}}{H_z^c}\left(\frac{\partial c}{\partial s}\right)\right] , \tag{34}$$

where C includes both non-wave and wave-enhanced turbulent mixing parameterizations (Sec. 3.4) and $\mathcal{E}$ is defined in (6).

The wave model is solved before the predictor stage for the baroclinic mode (Shchepetkin and McWilliams, 2005), and subsequently the WEC components are computed. For 3D simulations these are kept unchanged during the barotropic time steps; for 2D simulations, however, the WKB wave model is solved at every barotropic time step, and the WEC terms are updated as ζ^c and $\overline{\mathbf{u}}$ evolve. All the new terms associated with the conservative WEC are discretized with the centered finite-differences in a manner similar to the other terms in ROMS at the predictor and corrector stages. The vertical VF in (33) is discretized with the density-Jacobian scheme (Blumberg and Mellor, 1987) to reduce the terrain-following-coordinate error. Correction of $(\mathbf{u}^\ell, \omega^\ell)$ with the updated Stokes velocity occurs before the corrector steps. These procedures enable us to minimize the code changes in ROMS. Notice that the prognostic variables in ROMS with WEC are composite sea level ζ^c and Eulerian velocity $(\mathbf{u}, \omega)$.

3.2. Non-Conservative Wave Dissipation and Rollers

The primary wave dissipation rate in (15) is calculated as the sum of the effects of wave breaking ϵ^b and wave bottom drag ϵ^{wd},

$$\epsilon^w = \epsilon^b + \epsilon^{wd} \,. \tag{35}$$

These wave dissipation processes also imply WEC accelerations (Sec. 3.3).

Bottom viscous drag on the primary waves causes a dissipation ϵ^{wd} and an associated wave-averaged bottom stress $\boldsymbol{\tau}^{wd}_{bot} = \epsilon^{wd}\mathbf{k}/\sigma$ that induces an Eulerian bottom streaming flow in the direction of wave propagation (Longuet-Higgins, 1953). We use a parameterization by Reniers et al. (2004b) for the realistic regime of a turbulent wave boundary layer, which is based on the Rayleigh wave height distribution in accordance with Thornton and Guza (1983) consistent with the present WKB spectrum-peak wave modeling:

$$\epsilon^{wd} = \frac{1}{2\sqrt{\pi}} \rho_0 f_w |\mathbf{u}^w_{orb}|^3 \,, \tag{36}$$

where $|\mathbf{u}^w_{orb}| = \sigma H_*/(2\sinh kD)$ is bottom wave orbital velocity, and f_w is a wave friction factor (Soulsby, 1997),

$$f_w = 1.39 \left(\frac{\sigma z_o}{|\mathbf{u}^w_{orb}|} \right)^{0.52} \,. \tag{37}$$

Wave dissipation due to wave breaking ϵ^b is a combination of deep-water breaking (*e.g.*, white-capping) and depth-induced nearshore breaking. Deep-water breaking in wind-wave equilibrium is integrally equivalent to the surface wind stress (Sullivan et al., 2007); in this paper for simplicity we will use the latter representation (consistent with ignoring wave generation in the monochromatic wave model in Sec. 2.4). However, the depth-induced breaking is essential for surf zone wave-current interaction. A parameterization (Thornton and Guza, 1983) is

$$\epsilon^b = \frac{3\sqrt{\pi}}{16} \rho_0 g \frac{B_b^3 f_p}{\gamma_b^4 D^5} H_*^7 \,, \tag{38}$$

where f_p is a peak wave frequency ($1/T_p = \omega/2\pi$ with T_p a peak wave period), $H_* = 2A$ (Sec. 2.4), and B_b and γ_b are empirical parameters related to breaker types. An alternative parameterization by Thornton and Whitford (1990) is described by Church and Thornton (1993):

$$\epsilon^b = \frac{3\sqrt{\pi}}{16} \rho_0 g \frac{B_b^3 f_p}{D} H_*^3 \left[1 + \tanh\left\{ 8 \left(\frac{H_*}{\gamma D} - 1 \right) \right\} \right] \left[1 - \left\{ 1 + \left(\frac{H_*}{\gamma_b D} \right)^2 \right\}^{-\frac{5}{2}} \right] \,, \tag{39}$$

where B_b and γ_b are again empirical constants depending on types of breaking. In the DUCK94 simulation the latter parameterization is found to be more successful (Sec. 4).

To better estimate surf zone currents, an additional wave component is sometimes included (Svendsen, 1984a), *i.e.*, surface rollers, which are onshore-traveling bores of broken primary waves. The idea is that some fraction α_r is converted into rollers that propagate toward the shoreline before dissipating, while the remaining fraction $1-\alpha_r$ causes local dissipation (hence current acceleration). Here we introduce a surface roller model by primarily following Nairn et al. (1991) and Reniers et al. (2004a) with minor modifications. The roller is assumed to have the same $\mathbf{k}$ as the breaking primary wave in (14). The evolution equation for the roller action density $\mathcal{A}^r$ is analogous to (15) for $\mathcal{A}$:

$$\frac{\partial \mathcal{A}^r}{\partial t} + \nabla\cdot(\mathcal{A}^r\mathbf{c}) = \frac{\alpha_r\epsilon^b - \epsilon^r}{\sigma}\,, \tag{40}$$

where $\mathcal{A}^r = E^r/\sigma$; E^r is roller energy density; and $\mathbf{c} = \overline{\mathbf{u}} + \sigma k^{-2}\mathbf{k}$ is the phase speed of the primary wave (not $\mathbf{c}_g$; Svendsen, 1984a; Stive and De Vriend, 1994). While most previous studies, including Svendsen (1984a), Nairn et al. (1991) and Apotsos et al. (2007), assume that the full primary wave ϵ^b feeds the roller energy density (*i.e.*, $\alpha_r = 1$), Tajima and Madsen (2006) introduce α_r, $0 \le \alpha_r \le 1$. We view the latter as useful for correcting ϵ^b with some flexibility to depict different breaking wave and beach forms (*e.g.*, spilling or plunging breakers, barred or plane beaches); however, its value is an *ad hoc* choice. The roller dissipation rate is then parameterized as

$$\epsilon^r = \frac{g\sin\beta E^r}{c}\,. \tag{41}$$

where $\sin\beta = 0.1$ is an empirical constant (Nairn et al., 1991; Reniers et al., 2004a). According to Svendsen (1984a), the roller Stokes transport for a monochromatic primary wave is

$$\mathbf{U}^r = \frac{E^r}{\rho_0\,\sigma}\mathbf{k} = \frac{\mathcal{A}^r}{\rho_0}\mathbf{k}\,, \tag{42}$$

hence the total Stokes transport is

$$\mathbf{U}^{St} = \frac{(E+E^r)}{\rho_0\,\sigma}\mathbf{k} = \frac{(\mathcal{A}+\mathcal{A}^r)}{\rho_0}\mathbf{k}\,. \tag{43}$$

We assume that $\mathbf{U}^r$ is vertically distributed similarly to the Stokes drift velocity of the primary waves, hence

$$\mathbf{u}^{St}(z) = \frac{\sigma^2\cosh 2k(z+h)}{g\,\sinh^2 kD}\,(\mathcal{A}+\mathcal{A}^r)\,\mathbf{k}\,. \tag{44}$$

The expression for primary-wave Stokes drift in (44) is for non-breaking, small-slope waves that may not be accurate in the surfzone. We also assume for simplicity that (44) is applicable to the roller Stokes drift, although NA07b represented it with a surface-intensified vertical structure. (The same assumption about (44) for the roller waves is also made in other models such as the Lagrangian-mean radiation-stress model by W08.) There is room for future investigation.

A coupled wave simulation model such as SWAN (Booij et al., 1999) provides $\mathbf{k}_p$, σ_p, $H_{sig} = \sqrt{2}H_*$, $\overline{\epsilon^b}$, $\overline{\epsilon^{wd}}$, and Q_s, where Q_s is the fraction of broken waves ($0 \le Q_s \le 1$). As originally given by Svendsen (1984a), with consideration of Q_s, the roller action density is then

$$\mathcal{A}^r = \frac{E_r}{\sigma} = \frac{\rho_0\,g\,D\,A_R}{2\,L_p\,\sigma_p}\,Q_s\,, \tag{45}$$

where L_p ($= 2\pi/|\mathbf{k}_p|$) is a primary wave length and A_R is a roller area in the vertical plane estimated from the formulas proposed by Svendsen (1984b) or Okayasu et al. (1986),

$$A_R = a_R^s H_*^2 \quad \text{or} \quad A_R = a_R^o H_* L_p \,, \tag{46}$$

with empirical constants $a_R^s = 0.9$ and $a_R^o = 0.06$. The latter is adopted to shift the peak undertow velocity farther shoreward under plunging waves.

3.3. Non-Conservative Wave Accelerations for Currents

The wave dissipation processes (ϵ^b, ϵ^r, and ϵ^{wd} in Sec. 3.2) have accompanying WEC accelerations $\mathbf{A}^w$ (*e.g.,* Dingemans et al., 1987). We distinguish $\mathbf{A}^w$ from the wave-enhanced turbulent vertical mixing $\mathbf{D}^w$ and bottom drag stress $\boldsymbol{\tau}_{bot}^{cd}$ discussed in Sec. 3.4. Thus,

$$\mathbf{F}^w = \mathbf{A}^w + \mathbf{D}^w \,, \qquad \mathbf{A}^w = \mathbf{B}^b + \mathbf{B}^{wd} \,; \tag{47}$$

for brevity $\mathbf{B}^b$ contains both the depth-induced breaking and roller accelerations. We represent the accelerations either as body forces or as equivalent boundary stresses if the associated turbulent boundary layers are too thin to be resolved in a particular model configuration. For simplicity we revert to Cartesian coordinates in the rest of this section, with implied translation into transformed coordinates for ROMS along the lines indicated in Sec. 3.

The breaking and roller accelerations enter as a body force through $\mathbf{F}^w$ in the current momentum equations (26) - (27). They are expressed as

$$\mathbf{B}^b = \frac{(1-\alpha_r)\,\epsilon^b + \epsilon^r}{\rho_0 \sigma} \mathbf{k}\, f^b(z) \,, \tag{48}$$

where $f^b(z)$ is a vertical distribution function representing vertical penetration of momentum associated with breaking waves and rollers from the surface. It is normalized as

$$\int_{-h}^{\zeta^c} f^b(z')dz' = 1 \,, \tag{49}$$

hence the vertical average of $\mathbf{B}^b$ (*i.e.,* barotropic acceleration) is

$$\overline{\mathbf{B}}^b = \frac{(1-\alpha_r)\,\epsilon^b + \epsilon^r}{\rho_0 \sigma D} \mathbf{k} \,. \tag{50}$$

We can alternatively incorporate the breaking acceleration as an equivalent surface stress boundary condition for $\mathbf{u}$ instead of a body force (*e.g.,* as done in NA07):

$$\boldsymbol{\tau}_{sur} = \boldsymbol{\tau}_{sur}^{wind} + \boldsymbol{\tau}_{sur}^{b} \,, \tag{51}$$

where $\boldsymbol{\tau}_{sur}^{wind}$ is the usual oceanic-model representation of surface wind stress and

$$\boldsymbol{\tau}_{sur}^{b} = \rho_0 D \overline{\mathbf{B}}^b \tag{52}$$

is the stress due to primary wave breaking and rollers. To examine the sensitivity to the choice of f^b, we consider three alternative shapes:

$$\begin{aligned} \text{type I} \quad &: \quad f^b(z) \propto 1 - \tanh\left[k_b\,(\zeta^c - z)\right]^4 \,, \\ \text{type II} \quad &: \quad f^b(z) \propto 1 - \tanh\left[k_b\,(\zeta^c - z)\right]^2 \,, \quad \text{and} \\ \text{type III} \quad &: \quad f^b(z) \propto \cosh\left[k_b\,(z+h)\right] \end{aligned} \tag{53}$$

(leaving out the normalization factors for (49)). The vertical length scale k_b^{-1} controls the penetration depth in each of these shape functions. Usually we represent $k_b^{-1} = a_b H_*$, where a_b is an $O(1)$ constant. The first f^b in (53) is proposed in W08 to account for the depth-dependent radiation stresses divergence associated with rollers; the second one is an alternative that concentrates the breaking effects nearer the surface; and the last one is inspired by the structure of the primary wave and further matches the vertical scale of its velocity variance with $k_b = 2k$ (*i.e.,* a choice based on wavelength not wave amplitude).

Wave-induced bottom streaming (Longuet-Higgins, 1953; Xu and Bowen, 1994) is similarly represented as a body force:

$$\mathbf{B}^{wd} = \frac{\epsilon^{wd}}{\rho_0 \sigma} \mathbf{k} f^{wd}(z)\,, \tag{54}$$

where $f^{wd}(z)$ is a vertical distribution function normalized as in (49) for the Reynolds stress divergence associated with the turbulent wave bottom boundary layer (WBBL). We employ three upward decaying functions f^{wd} analogous to f^b,

$$\begin{aligned} \text{type I} \quad &: \quad f^{wd}(z) \propto 1 - \tanh\left[k_{wd}\,(h+z)\right]^4\,, \\ \text{type II} \quad &: \quad f^{wd}(z) \propto 1 - \tanh\left[k_{wd}\,(h+z)\right]^2\,, \quad \text{and} \\ \text{type III} \quad &: \quad f^{wd}(z) \propto \cosh\left[k_{wd}\,(\zeta^c - z)\right]\,, \end{aligned} \tag{55}$$

with a decay length $k_{wd}^{-1} = a_{wd}\delta_w$. a_{wd} is a constant, and δ_w is the WBBL thickness,

$$\delta_w = 0.09 k_N \left(\frac{A_{orb}^w}{k_N}\right)^{0.82}\,. \tag{56}$$

$A_{orb}^w = |\mathbf{u}_{orb}^w|/\sigma$ is a semi-orbital excursion of short waves; $k_N = 30\,z_o$ is the Nikuradse roughness; and z_o is roughness (Fredsøe and Deigaard, 1995); δ_w is typically only a few cm. $a_{wd} = 1$ corresponds to the theoretical turbulent WBBL thickness associated with monochromatic waves, whereas it is known that there exists a significant increase in a_{wd} under random waves based on laboratory measurements (Klopman, 1994); *e.g.,* Reniers et al. (2004b) use $a_{wd} = 3$. Its depth integral has an equivalent effect to a bottom stress,

$$\boldsymbol{\tau}_{bot}^{wd} = \rho_0 D \overline{\mathbf{B}}^{wd} = \frac{\epsilon^{wd}}{\sigma}\mathbf{k}\,. \tag{57}$$

When k_{wd}^{-1} is too thin to be resolved on the model grid, then the streaming acceleration is applied only as a stress in the bottom grid cell.

This formula implies bottom streaming occurs in the direction of wave propagation, consistent with the viscous streaming in laminar (Longuet-Higgins, 1953) and weakly turbulent (Longuet-Higgins, 1958) regimes under sinusoidal forcing. In contrast, nonlinear waves with the second-order Stokes theory and asymmetric forcing in rough turbulent WBBLs reduce the Longuet-Higgins positive streaming, and under some circumstances even manifest opposite flow (*e.g.,* Trowbridge and Madsen, 1984; Davies and Villaret, 1999). In the surf zone near-bed undertow opposite to the incident waves dominates over streaming (Sec. 4.6).

There could additionally be a surface streaming flow due to a wave-viscous boundary layer in a thin layer of thickness, $\sqrt{2\nu/\sigma} \approx 1$ mm, where ν is the molecular viscosity (Longuet-Higgins, 1953), but we take the view that it is negligibly small, especially in the presence of wave breaking.

3.4. Wave-Enhanced Vertical Mixing

In ROMS the parameterization of vertical mixing is often done in the framework of the non-local, first-order turbulent closure model, K-Profile Parameterization, KPP (Large et al., 1994; Shchepetkin and McWilliams, 2010). Apart from wave effects KPP comprises a shear-convective surface boundary layer (with counter-gradient flux as well as eddy diffusion), a shear bottom boundary layer, and interior mixing due to stratified shear instability, breaking internal waves, and double diffusion. In the KPP formulation for eddy diffusivity K_v, the effects of different mixing processes are mostly superimposed as if they were independent. Exceptions are that the boundary-layer rule for K_v overrides the interior rule within the boundary layers and that in shallow locations where the surface and bottom boundary layers overlap, we choose the local maximum value for the eddy diffusivity, $K_v(z) = \max[K_{v\,sur}(z),\ K_{v\,bot}(z)]$ (Durski et al., 2004; Blaas et al., 2007). It is likely that the different mixing processes sometimes combine nonlinearly, so we view the present approach as a preliminary one that has the advantage of process completeness but should be reconsidered when more is known.

In the WEC implementation K_v is augmented by wave-induced mixing in both the surface and bottom boundary layers. The incremental wave-enhanced momentum mixing of momentum is due to surface breaking (b) and bottom current drag (cd):

$$\mathbf{D}^w = \frac{\partial}{\partial z}\left[\left(K_v^b(z) + K_v^{cd}(z)\right)\,\frac{\partial \mathbf{u}}{\partial z}\right], \tag{58}$$

plus an equivalent diffusivity for tracers. In the surface region, K_v^b is added to $K_{v\,sur}$, by the rationale in the preceding paragraph. In the bottom boundary layer K_v^{cd} is a generalization for the usual KPP $K_{v\,bot}(z)$ because of the wave-enhanced bottom stress.

Mixing near the surface due to breaking has been modeled with local turbulent closures. Craig and Banner (1994) propose a model based on the Mellor-Yamada level 2.5 closure model (Mellor and Yamada, 1982; Galperin et al., 1988) by introducing a turbulent kinetic energy input at the surface and a modified surface roughness scale with a prescribed bilinear relationship for the turbulent length scale analogous to the law of the wall. Subsequently this approach has been further developed (Burchard, 2001; Umlauf et al., 2003; Newberger and Allen, 2007b; Jones and Monismith, 2008). We take a similar approach by defining $K_v^b(z)$ consistent with the depth-averaged eddy viscosity proposed by Battjes (1975) and vertically distributed with a shape function $f^{Kv}(z)$ (analogous to f^b in Sec. 3.3):

$$K_v^b(z) = c_b\left(\frac{(1-\alpha_r)\,\epsilon^b + \epsilon^r}{\rho_0}\right)^{1/3} H_*\,D\,f^{Kv}(z)\,, \tag{59}$$

where c_b is a constant[3]. This can be viewed as mixing-length estimate, with the velocity scale based on the breaker dissipation rate and the length scale based on the local wave height H_*, modified by the vertical distribution function $f^{Kv}(z)$ and with the depth factor D to retain the depth-average value of Battjes (1975). Apotsos et al. (2007) use $c_b = 1/14$ based on deep-water wave dissipation measured by Terray et al. (1996), so we anticipate c_b is an $O(0.1)$ parameter. Terray et al. (1996) report that the penetration depth of surface turbulence is proportional to the wave height, with little reduction in turbulent intensity to a depth of $0.7H_*$. Hence, the depth-dependency of K_v^b can be slightly different from that of $\mathbf{B}^b$. To allow distinct vertical scaling for $\mathbf{B}^b$ and K_v^b, we will define a vertical scale for K_v^b with $k_{Kv}^{-1} = a_{Kv}H_*$, where k_{Kv} replaces k_b in (53) and a_{Kv} is an $O(1)$ parameter.

[3]There is disagreement among local-closure modelers about the shape of K_v^b near the surface, primarily because of different assumptions about the length scale profile; *e.g.,* Burchard (2001) has K_v^b decrease as $z \to \zeta^c$, while Jones and Monismith (2008) has it increase. Our choice of f^{Kv} is monotonically increasing, essentially for profile simplicity. These distinctions probably matter only on a finer vertical scale (*i.e.,* a fraction of H_*) than we should expect our model to be apt.

Table 1: Common Model Parameters for DUCK94 Simulations

variable	value	unit
offshore wave height H_*	1.6	m
offshore peak wave period T_p	6.0	s
offshore incident wave angle θ_o	193.0	degree
CT93 breaking parameter B_b	0.64	–
CT93 breaking parameter γ_b	0.31	–
roller dissipation parameter $\sin\beta$	0.1	–
offshore tidal elevation ζ_{tide}	0.7	m
cross-shore wind stress $\tau_{sur}^{wind,x}$	-0.2532	Pa
alongshore wind stress $\tau_{sur}^{wind,y}$	-0.1456	Pa
Coriolis frequency f	8.5695×10^{-5}	1/s
lateral momentum diffusion coefficient K_h	0.1	m^2/s
mean water density ρ_0	1027.5	kg/m^3

In the bottom boundary layer due to current shear turbulence, wave motions enhance the bottom shear; *e.g.*, Soulsby (1995) proposes the drag law,

$$\boldsymbol{\tau}_{bot}^{cd} = \boldsymbol{\tau}_c \left[1.0 + 1.2 \left(\frac{|\tau_w|}{|\tau_w| + |\boldsymbol{\tau}_c|} \right)^{3.2} \right],$$
$$\boldsymbol{\tau}_c = \rho_0 \left[\frac{\kappa}{\ln(z_m/z_o)} \right]^2 |\mathbf{u}|\mathbf{u} \; ; \quad |\tau_w| = \frac{1}{2} \rho_0 f_w |\mathbf{u}_{orb}^w|^2 \, , \tag{60}$$

where $\boldsymbol{\tau}_c$ and τ_w are bottom stresses due to current and waves; κ is the von Kármán constant; z_m is a reference depth above the bed, nominally equivalent to a half bottom-most grid cell height (in a barotropic model $z_m = D/2$; (*e.g.,* Uchiyama et al., 2009)); z_o is the bed roughness length; f_w is the wave friction factor given by (37); and $|\mathbf{u}_{orb}^w|$ is the bottom wave orbital velocity. As simpler alternatives for sensitivity testing, we define a linear bottom drag law,

$$\boldsymbol{\tau}_{bot}^{cd} = \rho_0 \mu \mathbf{u} \tag{61}$$

(μ is a linear drag coefficient [m/s]) and a log-layer drag law,

$$\boldsymbol{\tau}_{bot}^{cd} = \boldsymbol{\tau}_c = \rho_0 \left[\frac{\kappa}{\ln(z_m/z_o)} \right]^2 |\mathbf{u}|\mathbf{u} \tag{62}$$

(z_m and z_o are interpreted as in (60)). The magnitude of K_v^{cd} is proportional to $|\boldsymbol{\tau}_{bot}^{cd}|^{1/2}$ in a KPP bottom boundary layer scheme.

4. DUCK94 Experiment

For both model validation and dynamical interpretation, we simulate the vertical profile of horizontal velocity measured on a natural sandy beach at Duck, North Carolina, during the DUCK94 experiment (*e.g.,* Garcez Faria et al., 1998, 2000; Newberger and Allen, 2007b). The field data were obtained on October 12, 1994, when strong cross-shore currents were present associated with a storm. The vertical

Table 2: Computational configurations for the DUCK94 simulations. $\alpha_r = 0$ means no roller component. Options for bottom drag are the Soulsby model (60) S95, linear (61) LIN, and log-layer (62) LOG. Bottom roughness z_o [m] is used for S95 and LOG, while μ [m/s] is used for LIN. For f^b, f^{Kv}, and f^{wd}, roman numericals indicate the shape types defined in (53) and (55). a_b, a_{wd}, and a_{Kv} are length scale coefficients for the shape functions. S indicates use of the streaming stress model, either for surface breaking (52) or bottom streaming (57). SS denotes the Stokes scale, $k_b = 2k$.

	waves			bottom drag		$\mathbf{B}^b$		$\mathbf{B}^{wd}$		K_v^b			normalized R.M.S. errors	
Run	WEC	CEW	α_r	model	z_o or μ	f^b	a_b	f^{wd}	a_{wd}	f^{Kv}	a_{Kv}	c_b	u_{error}	v_{error}
1	ON	ON	1.0	S95	0.001	III	0.2	III	3.0	II	1.2	0.03	0.4270	0.0922
2	ON	ON	0.0	S95	0.001	III	0.2	III	3.0	II	1.2	0.03	0.7560	0.4277
3	ON	ON	1.0	S95	0.001	III	SS	III	3.0	II	1.2	0.03	0.8166	0.2422
4	ON	ON	0.0	S95	0.001	III	SS	III	3.0	II	1.2	0.03	0.8745	0.5582
5	ON	ON	0.25	S95	0.001	III	0.2	III	3.0	II	1.2	0.03	0.6518	0.2072
6	ON	ON	0.50	S95	0.001	III	0.2	III	3.0	II	1.2	0.03	0.5647	0.1113
7	ON	ON	0.75	S95	0.001	III	0.2	III	3.0	II	1.2	0.03	0.4896	0.0806
8	ON	OFF	1.0	S95	0.001	III	0.2	III	3.0	II	1.2	0.03	0.4096	0.0956
9	OFF	OFF	-	LOG	0.001	-	-	-	-	-	-	-	0.8952	0.6125
10	ON	ON	1.0	S95	0.001	III	0.1	III	3.0	II	1.2	0.03	0.4130	0.0965
11	ON	ON	1.0	S95	0.001	III	0.5	III	3.0	II	1.2	0.03	0.4617	0.0816
12	ON	ON	1.0	S95	0.001	III	1.0	III	3.0	II	1.2	0.03	0.5658	0.0945
13	ON	ON	1.0	S95	0.001	S	–	III	3.0	II	1.2	0.03	0.4336	0.0907
14	ON	ON	1.0	S95	0.001	III	0.2	III	3.0	I	1.2	0.03	0.4151	0.1028
15	ON	ON	1.0	S95	0.001	III	0.2	III	3.0	III	1.2	0.03	0.4001	0.2243
16	ON	ON	1.0	S95	0.001	III	0.2	III	3.0	II	0.4	0.03	0.6825	0.1397
17	ON	ON	1.0	S95	0.001	III	0.2	III	3.0	II	0.8	0.03	0.4829	0.1315
18	ON	ON	1.0	S95	0.001	III	0.2	III	3.0	II	1.6	0.03	0.4084	0.1456
19	ON	ON	1.0	S95	0.001	III	0.2	III	3.0	II	1.2	0.01	0.6019	0.1313
20	ON	ON	1.0	S95	0.001	III	0.2	III	3.0	II	1.2	0.05	0.4748	0.0961
21	ON	ON	1.0	S95	0.001	III	0.2	III	3.0	II	1.2	0.07	0.5256	0.1286
22	ON	ON	1.0	S95	0.001	III	0.2	III	3.0	II	1.2	0.10	0.5829	0.1818
23	ON	ON	1.0	S95	0.001	III	0.2	III	1.0	II	1.2	0.03	0.4317	0.0918
24	ON	ON	1.0	S95	0.001	III	0.2	III	5.0	II	1.2	0.03	0.4252	0.0926
25	ON	ON	1.0	S95	0.001	III	0.2	S	-	II	1.2	0.03	0.4346	0.0916
26	ON	ON	1.0	S95	0.001	III	0.2	OFF	-	II	1.2	0.03	0.4706	0.0924
27	ON	ON	1.0	S95	0.005	III	0.2	III	3.0	II	1.2	0.03	0.4520	0.3076
28	ON	ON	1.0	S95	0.010	III	0.2	III	3.0	II	1.2	0.03	0.5546	0.4532
29	ON	ON	1.0	LIN	0.004	III	0.2	III	3.0	II	1.2	0.03	0.4490	0.7508
30	ON	ON	1.0	LIN	0.008	III	0.2	III	3.0	II	1.2	0.03	0.4320	0.0865
31	ON	ON	1.0	LOG	0.001	III	0.2	III	3.0	II	1.2	0.03	0.4345	0.1893

profile of the littoral current was measured with a vertical stack of seven electromagnetic current meters (EMCs) mounted on a mobile sled at elevations of 0.41, 0.68, 1.01, 1.46, 1.79, 2.24 and 2.57 m above the bed. The sled was located at a sequence of sites along a cross-shore transect; each site sample lasted for 1 hour, and seven samples were made across the transect during the day. Horizontal velocity was also measured with a spatially-fixed cross-shore array of 11 EMCs distributed around the surf zone (*e.g.*, Feddersen et al., 1998). Directional wave spectra were measured on an alongshore line of 10 pressure sensors in 8 m depth (Long, 1996), and a cross-shore array of 13 pressure sensors was used to measure wave heights spanning the surf zone (Elgar et al., 1998). Further details of the data acquisition and processing are in Gallagher et al. (1996, 1998) and Elgar et al. (1998).

The vertical current profiles in DUCK94 have previously been modeled in NA07 using an Eulerian-averaged WEC model with a VF representation implemented within the POM code (Blumberg and Mellor, 1987). Their formulation is dynamically consistent within the shallow-water range, *i.e.*, $kh \ll 1$. It includes most of the necessary wave-induced forcing for nearshore applications, including conservative VF and quasi-static set-down as body forces; non-conservative forcing due to wave-breaking and associated surface roller as surface stresses; and wave-enhanced vertical mixing. A limitation of their model arises from the assumption of $kh \ll 1$, leading to neglect of the vertical variations in $\mathbf{u}^{St}$ and VF and distortion of the breaking acceleration profile.

We perform many simulations to expose 3D wave-current modeling sensitivities (Table 2). Run 1 is the baseline numerical experiment. It uses a type III shape function for $f^b(z)$ (53) with $a_b = 0.2$. The KPP modification by breaking relies on a type II shape function for $f^{Kv}(z)$ in (53) with $a_{Kv} = 1.2$ and $c_b = 0.03$. These choices represent breaking acceleration as a shallow, surface-intensified body force. For the bottom streaming acceleration, a type III shape is used for $f^{wd}(z)$ in (55) with $a_{wd} = 3.0$. Bottom

drag is with the combined wave-current model by Soulsby (1995) with $z_o = 0.001$ m (Feddersen et al., 1998). The wave field is evaluated by the WKB spectrum-peak model with surface roller ($\alpha_r = 1.0$), the empirical breaking parameterization (39), and the wave drag dissipation (36). CEW comprising the frequency Doppler shift and changes in mean water column height due to wave setup/down are included in the wave model unless otherwise stated. The wave model is tightly coupled with the current model at every ROMS baroclinic time step. We omit stratification (*i.e.*, constant temperature and salinity with no surface heat and freshwater fluxes). We specify a weak lateral momentum diffusion with a constant coefficient of 0.1 m^2/s to obtain smooth solutions. The imposed forcing due to waves, wind, and tides are averaged over the duration of the sled measurements and held constant during the simulations. Model parameters are summarized in Table 1.

The experiments in this section use the 3D code in a vertical ($x-z$) 2D mode by assuming alongshore y uniformity. The computational domain is chosen as 768 m in the cross-shore direction (x) with $\Delta x = 2$ m. For all runs 32 vertical s levels are used with grid-height refinement near the surface and bottom. The field-surveyed bottom topography with a bar around $x = 120$ m is used without any spatial smoothing. Alongshore topographic uniformity is assumed, and a periodic condition is imposed in the alongshore direction. A Neumann condition is applied at the shoreward boundary to allow mass and momentum exchange between the interior domain and the very shallow shoreward region ($x < 0$). Chapman-type radiation boundary conditions for ζ^c and $\overline{\mathbf{u}}$ are adapted at the offshore open boundary with weak nudging for ζ^c and $\overline{u}$ towards $\hat{\zeta} + \zeta_{tide}$ and $-\overline{u^{St}}$. A Neumann condition is used for all other variables at the offshore boundary. The baroclinic time step is 3 s with a mode-splitting ratio of 30. Simulations are initiated with a resting state and integrated for 6 hours to obtain steady solutions that are y-invariant (i.e., they are stable to littoral shear instability, consistent with the DUCK94 observations).

4.1. Waves and Depth-Averaged Currents

As background for the 3D simulations, we first examine two barotropic runs with and without the roller model (Runs 2d1 and 2d2). The cross-shore profiles of the wave field for Run 2d1 and the bottom topography are in Fig. 1a. The simulated $H_*(x)$ agrees reasonably well with the observed wave height (Elgar et al., 1998). The three dissipation terms in the wave model (Fig. 1b) demonstrate that depth-induced breaking ϵ^b occurs at two locations, around the bar crest and the nearshore region. The roller dissipation ϵ^r peaks slightly shoreward of ϵ^b by design. The frictional bottom streaming dissipation ϵ^{wd} is about one order of magnitude smaller than the others around the breaking points, but it is dominant in the offshore region ($x >$ 500 m). Because the WKB ray model is independent of the roller model, ϵ^b and ϵ^{wd} are identical in Run 2d2.

We compare the depth-averaged velocity, $\overline{\mathbf{u}} = (\overline{u}, \overline{v})$, and dynamic sea level, $\zeta^c - \zeta_{tide}$, among Runs 2d1-2d2 and two analogous 3D simulations (*i.e.,* Runs 1 and 2, with and without the roller model) in Fig. 1c - e. A roller has significant effects. The cross-shore velocity $\overline{u}$ is altered by the roller contribution to $\overline{u^{St}}$ because it must be an anti-Stokes flow in alongshore-uniform, steady-state solutions as required by barotropic mass conservation (Sec. 5.1; Uchiyama et al., 2009). The differences between 2D and 3D models are appreciable, more so in ζ^c and $\overline{v}$ than in $\overline{u}$. $\overline{v}$ generally increases towards the shore, particularly beyond the breaking point around the bar crest, and then it diminishes toward the shore. The roller pushes the peak $\overline{v}$ locations shoreward and weakens the cross-shore $\overline{v}$ gradient in the 2D and 3D cases. In the 3D runs, the peak $\overline{v}$ is reduced and the alongshore momentum is distributed further shoreward than the 2D cases, due to the bottom drag modification and vertical momentum imbalance via vertical mixing (Sec. 4.8). The 3D Run 1 with shallow breaking and roller provides the best agreement with the observed fixed-array $\overline{v}$ from Feddersen et al. (1998). Although $\overline{\mathbf{u}}$ and ζ^c vary in x, the resultant wave fields are nearly the same among the different cases, indicating that CEW plays a small role in

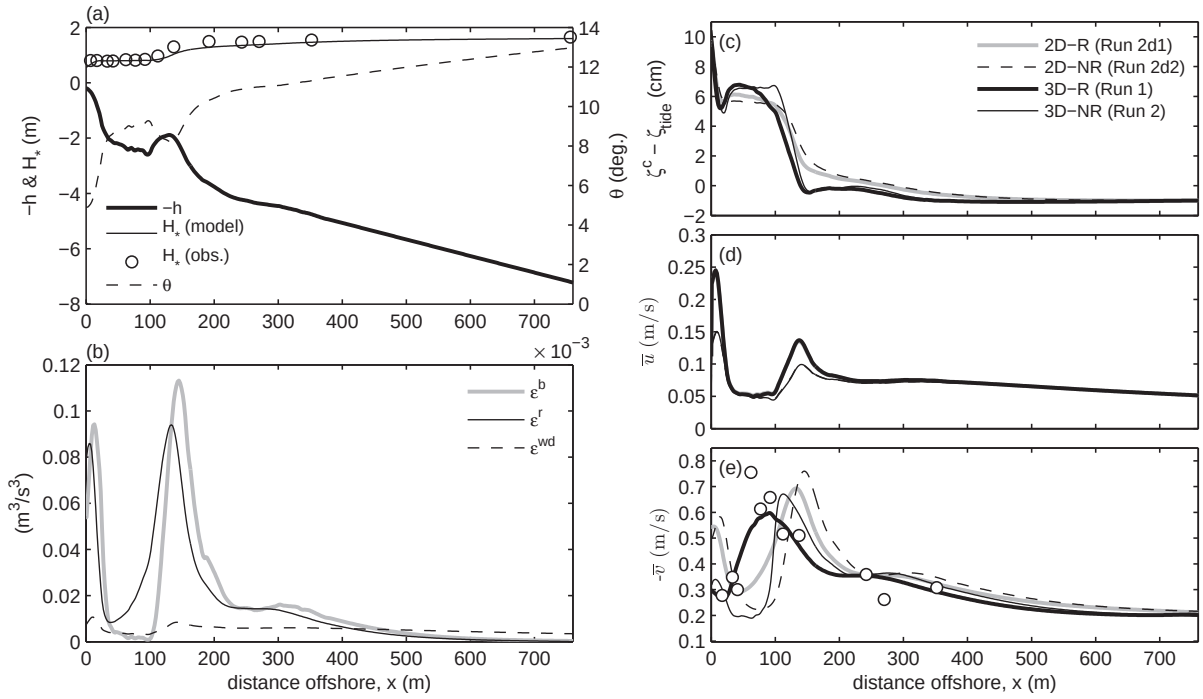

Figure 1: Cross-shore profiles of (a) resting depth h, wave height H_* (observed and modeled), and modeled wave angle θ; (b) ρ^{-1} times the wave dissipation rates by depth-induced breaking ϵ^b, roller ϵ^r, and bottom drag ϵ^{wd}; (c) ζ^c; (d) $\overline{u}$; and (e) $-\overline{v}$ along with the observed alongshore velocity from the fixed-array EMCs (circles) (Feddersen et al., 1998).

DUCK94 (in contrast to its much larger role in rip currents and littoral shear instabilities Yu and Slinn, 2003; Özkan-Haller and Kirby, 1999; Uchiyama et al., 2009).

4.2. Vertical Structure

To expose $\mathbf{B}^b$ depth-dependency and roller contributions in (48), we compare four 3D simulations (Runs 1 - 4; Table 2). Runs 1 and 2 have breaking as a shallow body force, while Runs 3 and 4 have a weaker depth variation in $\mathbf{B}^b$ by setting $k_b = 2k$ (*i.e.*, the same profile as $\mathbf{u}^{St}$) in (53); we call the latter runs deep breaking cases. The roller contribution is included in Runs 1 and 3 and absent in Runs 2 and 4. Figures 2 and 3 display ($\mathbf{u}$, w), ($\mathbf{u}^{St}$, w^{St}) and K_v for Run 1 in the $x-z$ plane (this case has the best match with the observed barotropic $\overline{v}$; Fig. 1e). $u(x,z)$ has a surf-zone overturning circulation with a strong onshore flow near the surface and an opposing, offshore undertow near the bottom. This circulation pattern is most prominent around the bar crest. The largest negative v appears in the trough region shoreward of the bar. An increase of K_v associated with an increase of K_v^b is observed around the bar and near the shoreward boundary (Fig. 3), consistent with the $\epsilon^b(x)$ profile (Fig. 1b). The 3D stokes velocities are strongest at these two breaking points, with depth-variation even in such a shallow area (Figs. 2d-f). u^{St} is much stronger than v^{St} by an order of magnitude due to the small obliqueness of the incident waves. The divergence implied by u^{St} induces two w^{St} dipole circulations, with wave-induced upwelling adjacent to the shoreline and inshore of the bar, and downwelling offshore of these locations. The vertical velocity w is comparable in magnitude to w^{St}, and its primary upwelling and downwelling centers occur in similar cross-shore locations, albeit more bottom-concentrated, *i.e.*, up- and downward flows on the inshore and offshore sides of the bar in the offshore-headed near-bed undertow. The vertical variation of $\mathbf{u}^{St}$ implies a depth-varying VF that leads to a simulation improvement compared to the

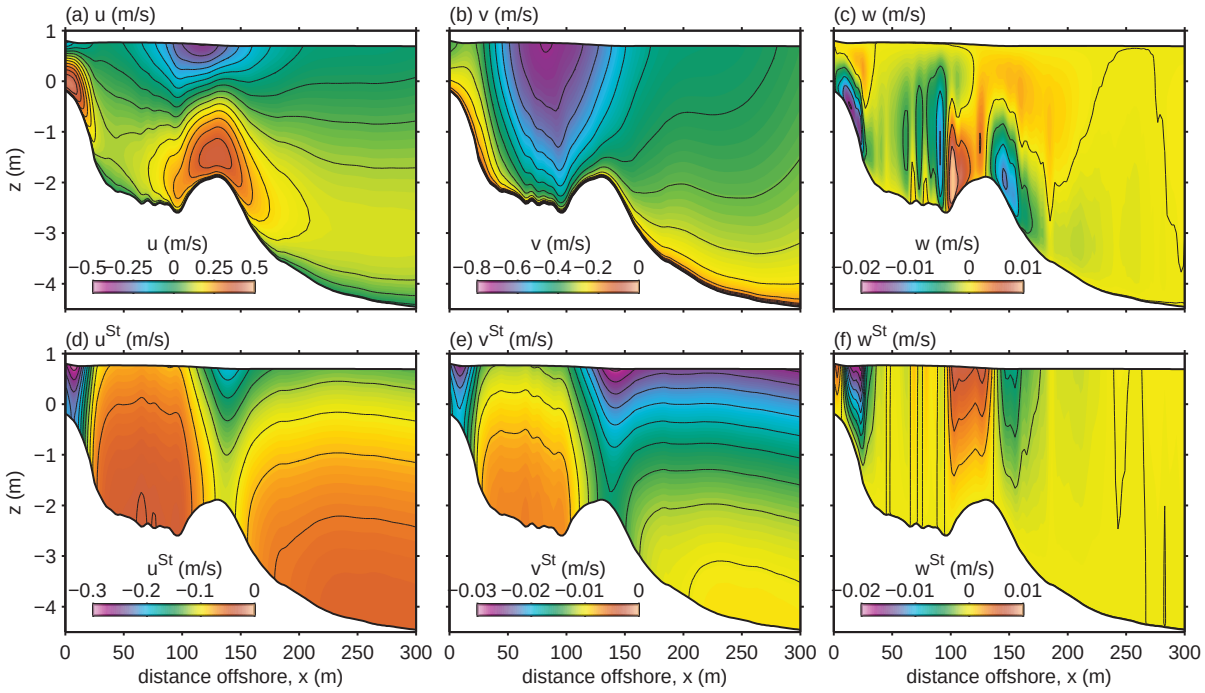

Figure 2: (a) Cross-shore velocity u, (b) alongshore velocity v, (c) vertical velocity w, (d) cross-shore Stokes velocity u^{St}, (e) alongshore Stokes velocity v^{St}, and (f) vertical Stokes velocity w^{St} for Run 1. Contour intervals are (a) 0.05 m/s, (b) 0.05 m/s, (c) 0.004 m/s, (d) 0.02 m/s, (e) 0.002 m/s and (f) 0.002 m/s.

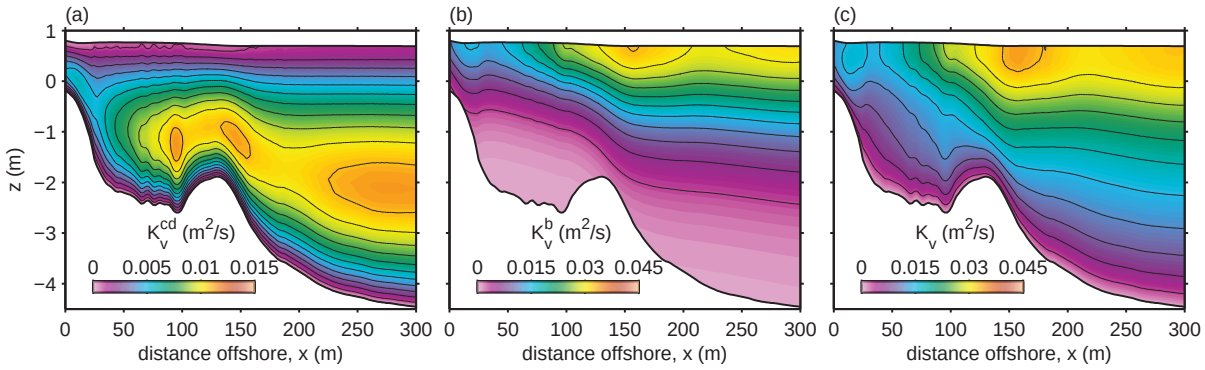

Figure 3: Distributions of vertical eddy viscosity for Run 1; (a) KPP contribution K_v^{cd}, (b) wave breaking contribution K_v^b and (c) $K_v = K_v^{cd} + K_v^b$. Notice that different color scales are utilized. Contour intervals are (a) 0.001 m^2/s, (b) 0.003 m^2/s, and (c) 0.003 m^2/s.

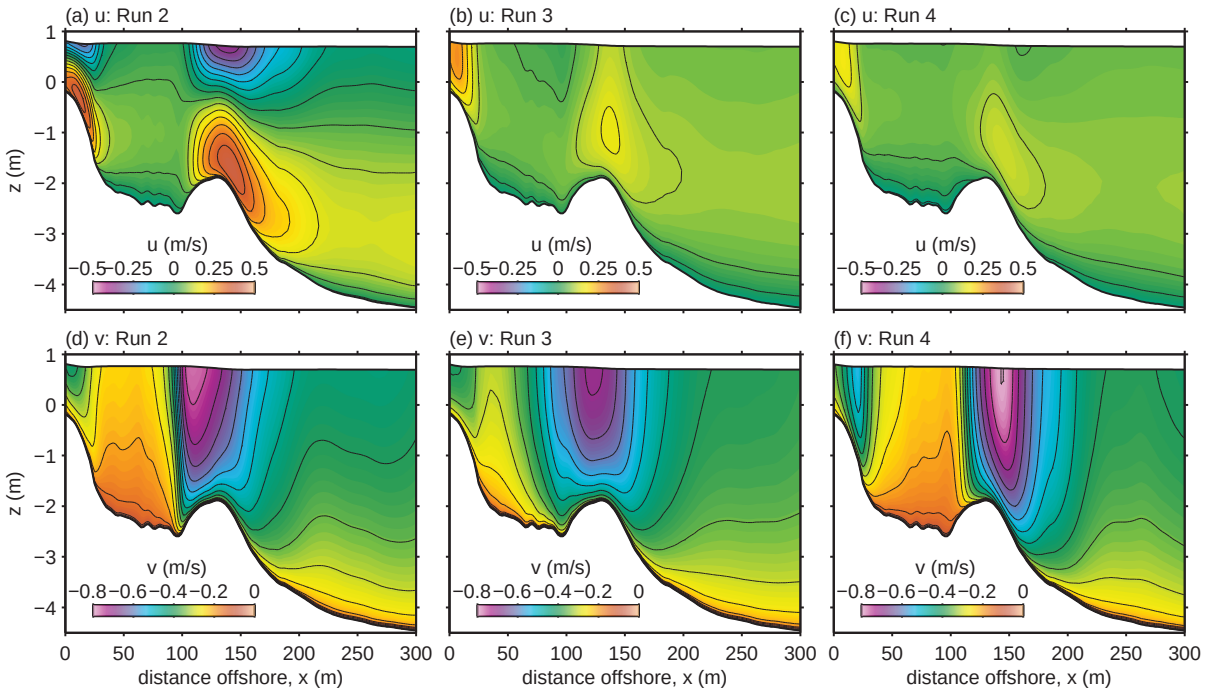

Figure 4: Distributions of u and v for shallow breaking without roller (Run 2; panels a and d); deep breaking with roller (Run 3; b and e); and deep breaking without roller (Run 4; c and f). Contour intervals are 0.05 m/s.

NA07 model (Sec. 4.8). The cross-shore undertow profile is modified significantly by the deep $\mathbf{B}^b$ (Figs. 4a-c). The surf-zone recirculation in u greatly weakens in Runs 3 and 4. Exclusion of the roller shifts the bar recirculation in u towards the shoreward trough region, then it increases the surface onshore u near the shoreward end. $v(x,z)$ is modified less than $u(x,z)$ among these runs (Figs. 4d-f), but the deep breaking acceleration tends to generate the peak v location near the bar crest and deeper than the shallow breaking cases. In turn, the roller acts to shift the peak v location shoreward, and v is mixed horizontally to reduce its cross-shore gradient.

Simulated $\mathbf{u}(x,z)$ fields are compared with the observed velocities (Garcez Faria et al., 1998, 2000) in Fig. 5, and the normalized r.m.s. errors for u and v (as defined in NA07b) at a total of 42 measurement positions are summarized in Table 2 (last two columns). The errors for Run 1 in matching the observations are generally the least. The deep breaking definitely lacks the recirculation pattern in u, with much weaker near-bed offshore undertow and near-surface onshore flow. All four 3D runs have fairly good agreement in v, while the exclusion of the roller clearly misses the increase of v in the trough region. As a consequence, both the shallow breaker forcing and the roller shift the peak v location shoreward, and the former acts to generate the recirculating u field quite well. The vertical structure of $\mathbf{u}$ and the r.m.s. errors for Run 1 ($u_{error} = 0.43$ and $v_{error} = 0.092$; Table 2) are similar to or a bit even better than those in NA07 where u_{error} and v_{error} range 0.45 – 0.70, and 0.12 – 0.50, respectively; nevertheless, we view NA07 as a generally skillful model of the shallow-water regime in DUCK94 ($kh < 1$). The K_v field from the modified KPP model (Fig. 3) has wave-enhanced structures both near the surface and at at mid-depth that influence the currents (Sec. 3.4). It is qualitatively similar to the K_v field in NA07 based on a two-equation local turbulence closure model with a modification due to wave breaking as in Craig and Banner (1994).

4.3. Effects of Waves

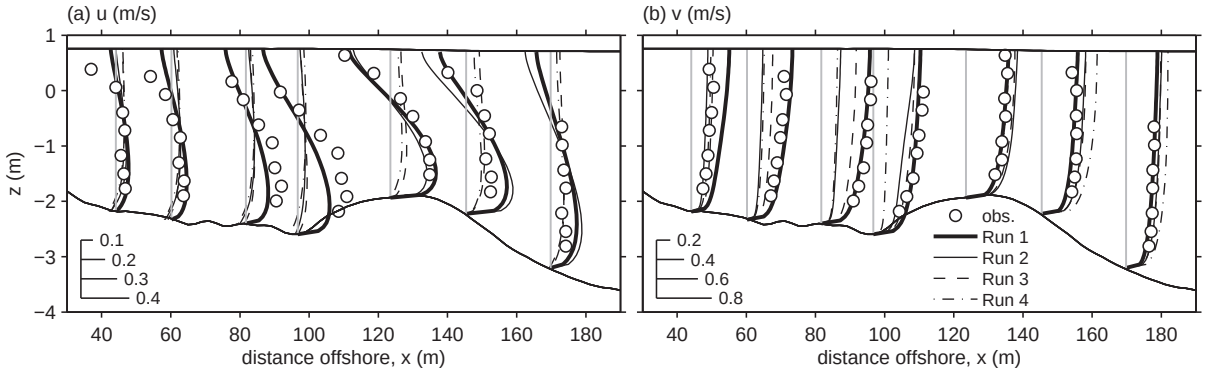

Figure 5: Model-data comparison in Runs 1 - 4 for (a) u and (b) v. The vertical thin axes indicate the measurement locations.

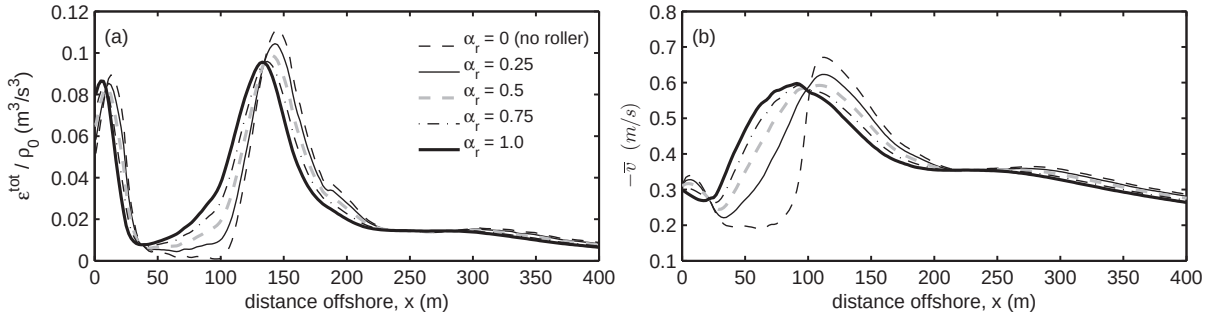

Figure 6: Cross-shore profiles of (a) combined breaking and roller dissipation ϵ^{tot} and (b) depth-averaged alongshore velocity $-\overline{v}$ for different α_r values (Runs 1, 2, and 5 - 7).

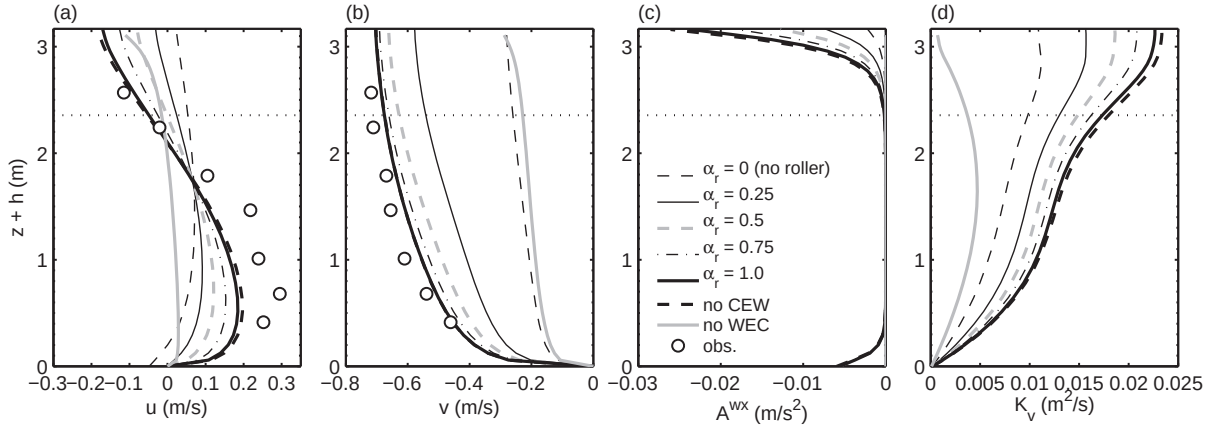

Figure 7: Model-data comparison in the trough region (x = 82 m) with different α_r values (Runs 1, 2, and 5 - 7) and without CEW (Run 8) or WEC (Run 9): (a) u, (b) v, (c) the cross-shore combined non-conservative breaking and bottom streaming forces A^{wx}, and (d) K_v. The horizontal dotted lines are at $z + h = D - H_*$ or $z = \zeta^c - H_*$.

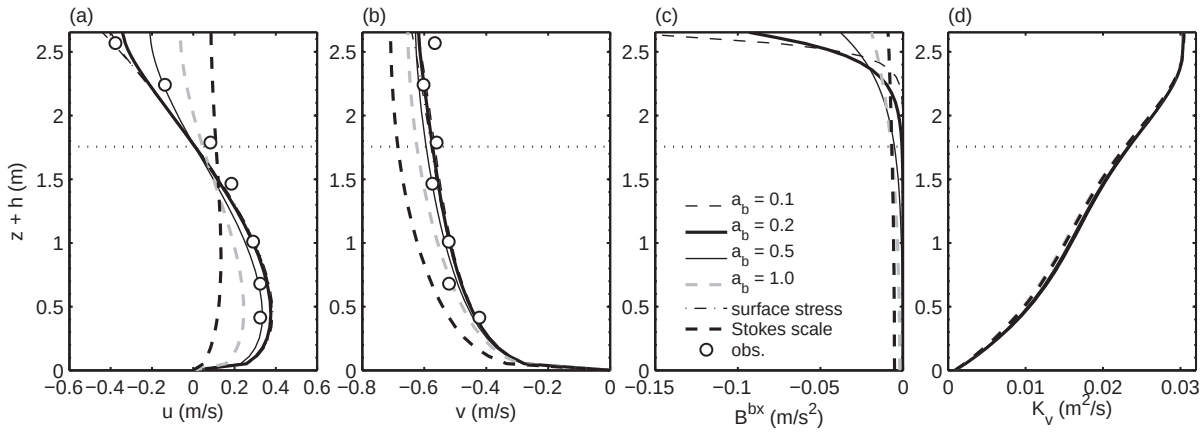

Figure 8: Model-data comparison varying $\mathbf{B}^b$ (Runs 1, 3, and 10 - 13) for (a) u and (b) v around the bar crest (x = 123 m); and modeled (c) $\mathbf{B}^{bx}$ and (d) K_v^b at x = 123 m. Horizontal dotted lines are at $z + h = D - H_*$ or $z = \zeta^c - H_*$.

The roller model can be viewed as a correction to ϵ^b (39) and $\mathbf{B}^b$ (48). We assess its influence by varying the value of α_r in (48) in 5 cases: Run 1: $\alpha_r = 1$; Run 2: $\alpha_r = 0$; Run 5: $\alpha_r = 0.25$; Run 6: $\alpha_r = 0.5$; and Run 7: $\alpha_r = 0.75$. As α_r increases, the peak $\epsilon^{tot} = (1 - \alpha_r)\epsilon^b + \epsilon^r$ location moves slightly shoreward, and ϵ^{tot} is noticeably intensified in the trough region, $50 < x < 100$ m (Fig. 6a). The $\overline{v}$ profiles gain more alongshore momentum in the trough with larger α_r (Fig. 6b). The vertical shears in $\mathbf{u}$ are also enhanced with larger α_r (Fig. 7a-b). This is due to an increase in the combined breaking and bottom streaming force A^{wx} (Fig. 7c). The changes in ϵ^{tot} alter the vertical eddy viscosity profiles (Fig. 7d), which are partly responsible for the $\mathbf{u}$ profiles. Thus, we confirm that a roller component greatly improves the match to DUCK94 (Garcez Faria et al., 1998, 2000, NA07b).

In Fig. 7 we show two additional cases that artificially restrict the wave-current interaction: Run 8 has no CEW in the WKB model, and Run 9 is entirely without WEC. Ignoring CEW does not have a large effect in this situation because the wave fields are not very different among our cases (Sec. 4.1). However, without WEC, both the recirculation in u and the flow in v are very weak, while K_v reverts to the KPP-evaluated K_v^{cd}; without wave-current interaction, the currents are entirely wind-driven. It is, of course, no surprise that WEC, especially due to $\mathbf{B}^b$, is a primary influence on littoral currents.

4.4. Depth-Dependent Breaking Acceleration

The vertical scale of $\mathbf{B}^b(z)$ set by k_b in (53) is crucial in the resultant surf-zone flow structure. Extending the runs in Sec. 4.2, we test 6 different settings for the breaking acceleration (Runs 1, 3, and 10 - 13 in Table 2). Runs 1 and 10 - 12 have a shallow breaking force with a type III function in (53) with different $k_b^{-1} = a_b H_*$: a_b = 0.1 (Run 10), 0.2 (Run 1), 0.5 (Run 11), and 1.0 (Run 12). Run 3 is for a deep $\mathbf{B}^b$ (*i.e.*, $k_b = 2k$). Run 13 specifies the breaking force as a surface stress as in (52).

For the smaller a_b and surface stress cases, u and v around the bar crest (x = 123 m) are rather alike and show a good agreement with the observations (Figs. 8a-b and the r.m.s. errors in Table 2), regardless of the different B^{bx} profiles (Fig. 8c). However, with larger a_b, the surface onshore and near-bed offshore undertow flows in u are significantly reduced, and the r.m.s. errors are much larger, while v is overestimated. The Stokes-scale f^b in Run 3 gives the worst agreement, and the shear in u is nearly absent. Vertical eddy viscosity K_v is substantially unaltered for all the cases (Fig. 8d). We conclude (consistent with NA07b) that a surface-concentrated $\mathbf{B}^b$ or an equivalent surface stress τ_{sur}^b is essential

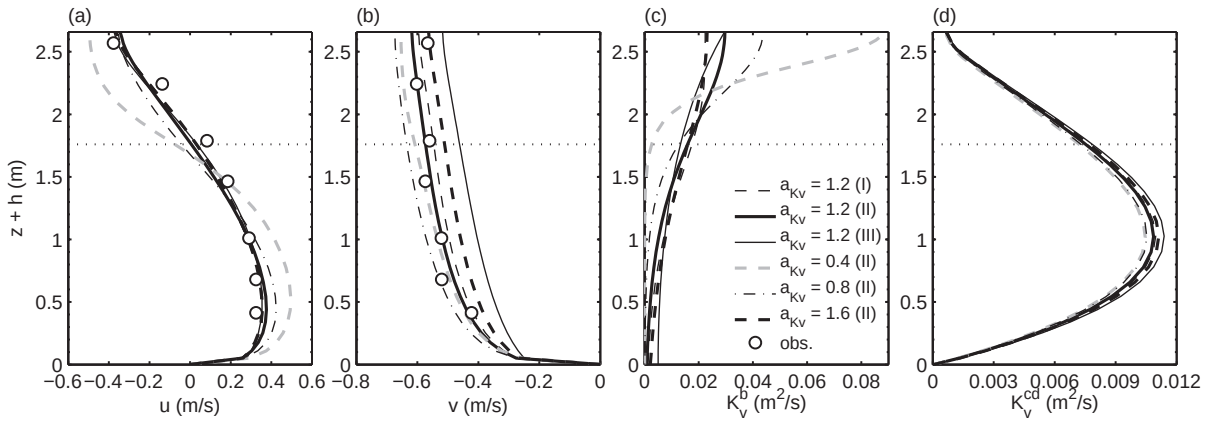

Figure 9: Sensitivity to wave-induced mixing (Runs 1 and 14 - 18) around the bar crest (x = 123 m): model-data comparisons for (a) u and (b) v and modeled (c) K_v^b and (d) K_v^{cd}. Roman numericals in parentheses in the legend in (c) indicate the shape types for f^{Kv} defined in (53). Horizontal dotted lines are at $D - H_*$.

to reproduce the surf-zone flow structure. We further test the sensitivity to the types of $f^b(z)$ function in (53), but find its influence on $\mathbf{u}(x,z)$ to be secondary to the choice of k_b.

4.5. Breaking Enhancement of Vertical Mixing

The wave breaking modification to KPP relies on a choice of the vertical shape function $f^{Kv}(z)$, its inverse scale a_{Kv}, and the parameter c_b (Sec. 3.4; (59)). We test their sensitivities by comparison of Run 1 (type II shape function, a_{Kv} = 1.2, c_b = 0.03) with Runs 14 - 15 (types I and III), Runs 16 - 18 (type II, a_{Kv} = 0.4, 0.8, and 1.6), and Runs 19 - 21 and 5 (type II, c_b = 0.01, 0.05, 0.07, and 0.1). Unlike with f^b, the diffusivity shape function has a noticeable influence, by underestimating v when type III is used and K_v^b exhibits less decay downward to the bed (Fig. 9). Similarly, as a_{Kv} increases the near-surface breaking effect deepens to intensify the near-bed K_v^b, while the KPP K_v^{cd} changes little among these cases. With smaller α_{K_v} the recirculating structure in u and magnitude in v are both strengthened. The empirical constant c_b in (59) also has moderate influence on the resultant $\mathbf{u}$ field (not shown). Its role is somewhat similar to that by a_{Kv}: decreasing c_b leads to stronger recirculation in u and to speed in v. (Notice that the Run 1 values that best fit DUCK94 (*i.e.*, a_{Kv} = 1.2 and c_b = 0.03) differ somewhat from the values suggested by Terray et al. (1996) and Apotsos et al. (2007) for deep-water waves (a_{Kv} = 0.7 and c_b = 0.07). We infer from the data comparisons that there is a greater sensitivity to the shape profile in K_v^b than in $\mathbf{B}^b$, and that the wave-induced mixing scale is significantly larger than the analogous breaking acceleration scale (*i.e.*, a_b = 0.2).

4.6. Bottom Streaming

Wave-induced bottom streaming (Sec. 3.3) has been less investigated than the other WEC mechanisms because it occurs within a thin wave bottom boundary layer (WBBL) that makes measurement and modeling difficult in the natural environment. We test the sensitivity to the non-dimensional length scale a_{wd} in (54)-(56) with Runs 23, 1 and 24 (a_{wd} = 1, 3 and 5, respectively), as well as Run 25 where the WBBL is unresolved and imposed as a bed stress as in (57) and Run 26 where streaming and bottom wave-drag dissipation are neglected with ϵ^{wd} = 0. The r.m.s. errors in Table 2 demonstrate exclusion of the streaming leads to a modest increase of model error, while the other cases yield approximately the same errors; however, there are few measurements near the bottom. The model-data comparison around

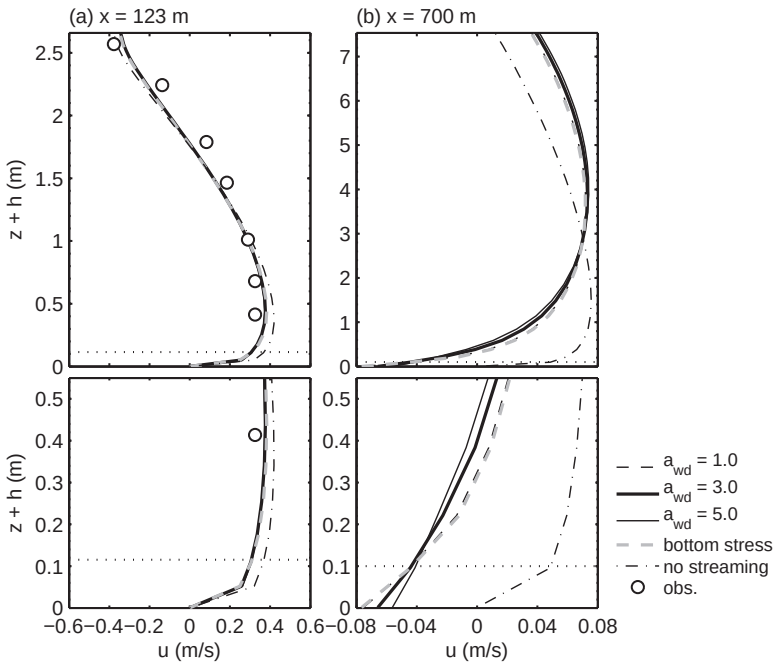

Figure 10: Model-data comparisons varying the bottom streaming (Runs 1 and 23 - 26) for u (a) around the bar crest at $x = 123$ m and (b) in the outer surf zone at $x = 700$ m. The upper panels are the vertical profiles for the entire water column, while the lower panels are a zoom near the bed. Horizontal dotted lines indicate the e-folding scale $k_{wd}^{-1} = a_{wd}\delta_w$ in the streaming body force shape function f^{wd}, with the particular value $a_{wd} = 3$.

the bar crest (Fig. 10a) shows that u is too strong without streaming because the near-bottom offshore flow is in the opposite direction to the onshore streaming stress. The streaming influence is even stronger in the offshore region with a wind-driven Stokes-Ekman flow (Fig. 10b); the streaming generates an onshore bottom velocity of 0.06 m/s and shifts the profile of u over the entire water column. Even in the offshore site, the sensitivity to the $\mathbf{B}^{wd}(z)$ (54) profile is modest (including to the function type in f^{wd}; not shown). The WBBL thickness δ_w in (56) is estimated as 0.04 ± 0.01 m, which is only marginally resolved with a bottom-most grid height that varies from 0.03 m at the shoreward boundary to 0.1 m at the offshore boundary. In other tests we have seen that marginal resolution, or even an unresolved bottom stress, is sufficient to capture the bulk effect of streaming on $\mathbf{u}(z)$. In offshore regions ϵ^{wd} typically dominates over ϵ^b, and its effect is known to be significant (Xu and Bowen, 1994; Lentz et al., 2008). It leads to a cross-shore bottom velocity convergence offshore of the bar crest in our simulations, and its associated sediment transport may help to maintain the bar structure in the surf zone.

4.7. Wave-Enhanced Bottom Drag

Bottom drag is well known to be the most important factor that determines barotropic alongshore velocity $\overline{v}$ (*e.g.,* Uchiyama et al., 2009). We examine its sensitivity on 3D $\mathbf{u}$ with alternative drag formulations: the combined wave-current model (60) with $z_o = 0.001$ m (Run 1), 0.005 m (Run 27) and 0.01 m (Run 28); the linear drag model (61) with $\mu = 0.004$ m/s (Run 29) and 0.008 m/s (Run 30); and the log-layer model (62) with $z_0 = 0.001$ m, omitting bed shear stress enhancement due to waves (Run 31). The vertical profiles of $\mathbf{u}$ around the bar crest (Fig. 11) vary substantially among these cases, as expected from barotropic modeling experience. Runs 1 and 30 lead to approximately equivalent flow fields with good model skills (Table 2). Increasing z_o with the Soulsby model increases model error by weakening the recirculation in u and reducing v. The linear drag model with small $\mu = 0.004$ and the

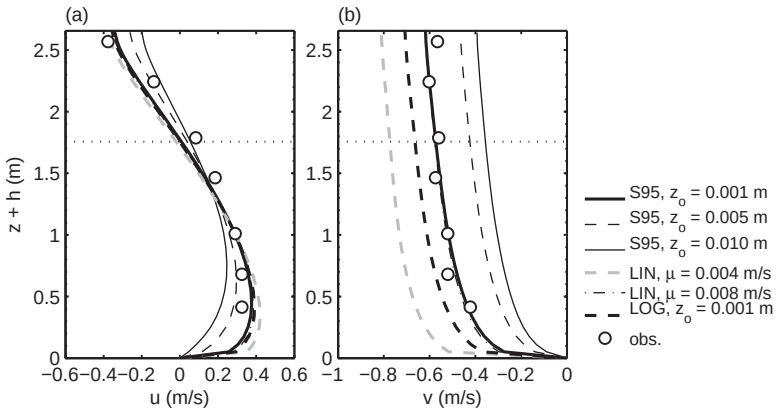

Figure 11: Model-data comparisons for the sensitivity to wave-enhanced bottom drag (Runs 1 and 27 - 31) around the bar crest (x = 123 m): (a) u and (b) v. Horizontal dotted lines are at $D - H_*$.

log-layer model yield good u profiles, but they have larger v than measured. Other sensitivities related to bottom drag are that $K_v(z)$ is slightly altered through CEW on K_v^b and bed shear stress on the KPP K_v^{cd} (not shown). Among the runs presented here, the Soulsby model with $z_o = 0.001$ m provides the best overall agreement with the data; the same conclusion was drawn with barotropic simulations of $\overline{v}$ for DUCK94 (Feddersen et al., 1998). In summary, bottom drag also plays a crucial role in the 3D structure of **u**.

4.8. Horizontal Momentum Balance

To diagnose the influential mechanisms in our 3D solutions, we analyze the momentum balances in Runs 1 - 3 (*i.e.*, the case that best matches Duck94, a case removing the roller, and a case increasing the vertical scale of the breaking acceleration). The advection and horizontal VF terms in (26) and (27) are rearranged into non-flux forms to separate the Eulerian advection $(\mathbf{u}\cdot\nabla)\mathbf{u}$ and the horizontal VF **J** in (5), which includes the Stokes-Coriolis force. The vertical VF K in (5) is extracted from the second term in the integral in (33) and added to the horizontal VF terms to combine them into the total VF terms. The horizontal gradient of the rest of (33) is the total pressure gradient force (PGF) $\mathbf{P}^{tot}$. We decompose the PGF into the non-WEC current contribution $\mathbf{P}^{c}$; the quasi-static response $\mathbf{P}^{qs}$; the Bernoulli head contribution $\mathbf{P}^{bh}$ from the interaction between vertical current shear and depth-dependent Stokes drift; and the WEC surface pressure boundary correction $\mathbf{P}^{pc}$:

$$\begin{aligned}\mathbf{P}^{tot} &= \mathbf{P}^{c} + \mathbf{P}^{wec} = \mathbf{P}^{c} + \mathbf{P}^{qs} + \mathbf{P}^{bh} + \mathbf{P}^{pc} \\ &= -\nabla_\perp\left(g\zeta^c + \int_{-h}^{z}\frac{g\rho}{\rho_0}\,dz\right) + g\nabla_\perp\hat{\zeta} + \nabla_\perp\mathcal{K}\,|_{\zeta^c} + \nabla_\perp\mathcal{P}\,|_{\zeta^c}\ . \end{aligned} \tag{63}$$

$\mathbf{P}^{wec} = \mathbf{P}^{qs} + \mathbf{P}^{bh} + \mathbf{P}^{pc}$ denotes the combined WEC contribution. All the momentum terms shown here are volume-averaged and placed on the right side of (26) and (27).

The barotropic cross-shore momentum balance in Fig. 12 is led by the pressure gradient ($\mathbf{P}^{tot}$) and breaking forces. This is consistent with the classical view of surf-zone momentum balance between wave-setup and breaking acceleration (*cf.,* Bowen et al., 1968; Raubenheimer et al., 2001). In the shallow breaking cases (Runs 1 and 2), the advection and the VF terms provide partially canceling cross-shore transports, whereas they are quite small in the deep breaking case (Run 3). Note that the cross-shore horizontal VF in Runs 1 and 2 is dominated by the vertical VF contribution. The alongshore momentum

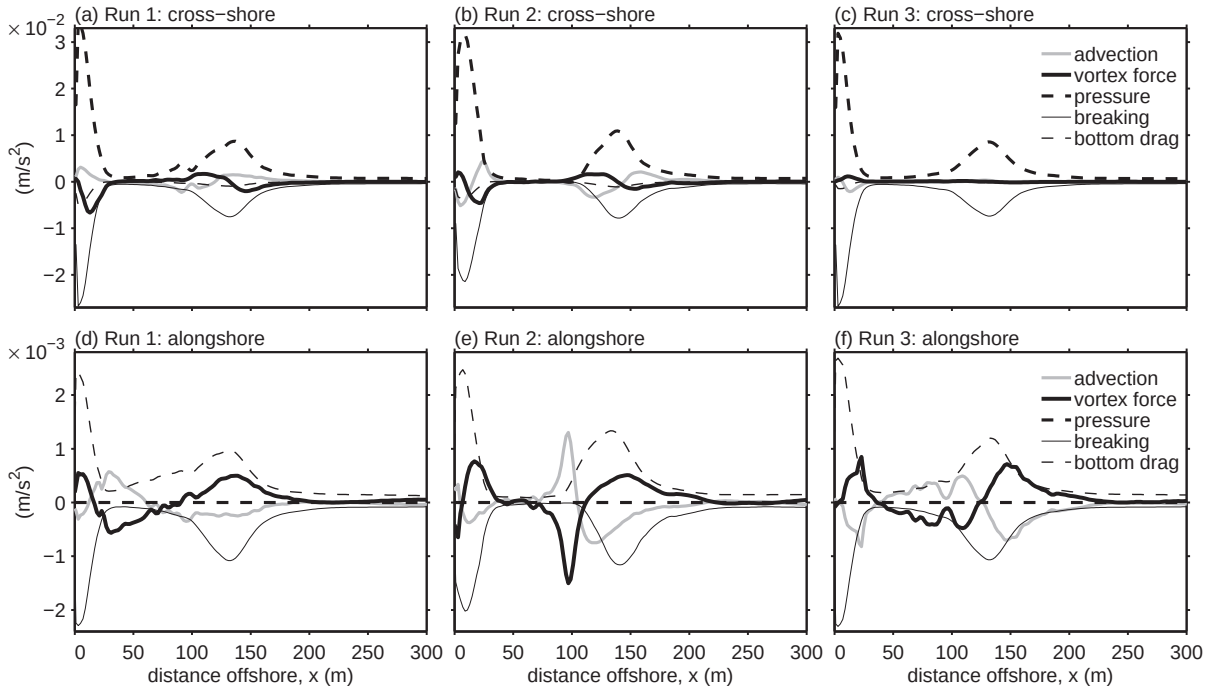

Figure 12: Depth-averaged (top) cross-shore and (bottom) alongshore momentum tendencies for Runs 1 (baseline case), 2 (no roller), and 3 (deep **B**).

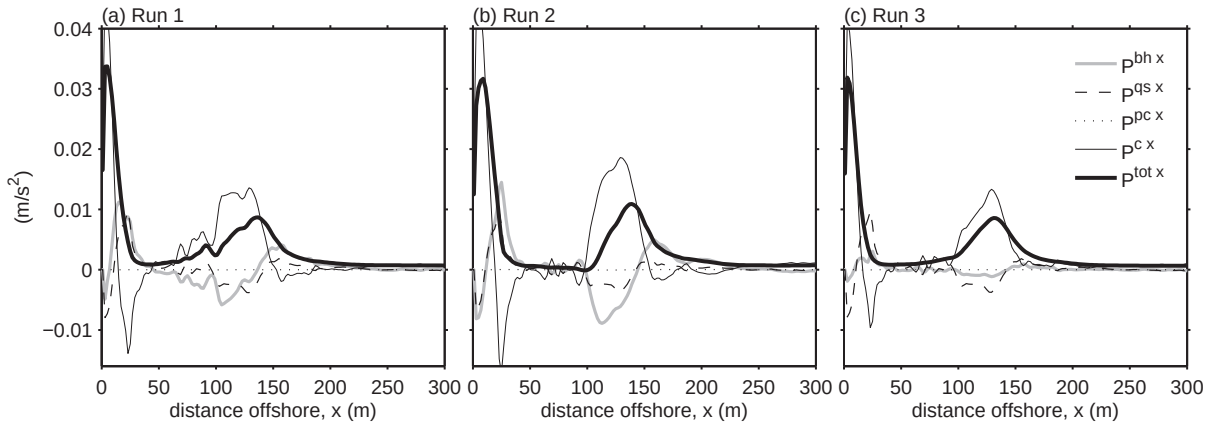

Figure 13: Depth-averaged cross-shore PGF decomposed as in (63) for Runs 1 - 3.

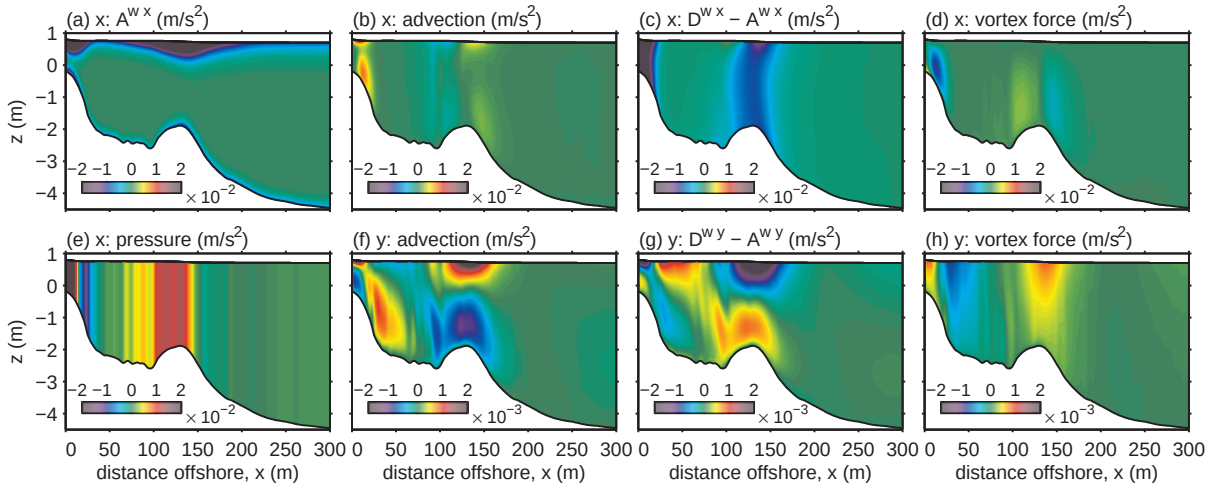

Figure 14: Leading terms in the 3D horizontal momentum balance for Run 1: (a) x wave acceleration A^{wx}, (b) x Eulerian advection, (c) x vertical mixing D^{wx}, (d) x total VF, (e) x PGF, (f) y Eulerian advection, (g) y vertical mixing D^{wy}, and (h) y total VF.

balance is led by the breaking acceleration and the bottom drag, again consistent with the classical view. There is a secondary balance between the advection and VF as required by the barotropic mass balance that results in the anti-Stokes $\overline{u}$ flow for an alongshore-uniform, steady circulation (Uchiyama et al., 2009). These secondary terms are again cross-shore transport, and they have a larger reach between the bar and the nearshore when the roller is present (Runs 1 and 3). The alongshore VF generally opposes $y-$advection where the latter is strong, but they are not completely canceled out, apparently because of different vertical structures of $\mathbf{u}$ and $\mathbf{u}^{St}$. The VF is also opposite to $B^{by} < 0$ around the bar region and near the shoreline, while accelerating $v < 0$ in the trough. The trough acceleration occurs in a more shoreward location with shallow breaking and roller (Run 1) than otherwise (Runs 2 - 3). In addition to the broader ϵ^{tot} in the trough with roller, the alongshore VF 3D shape is the reason why the peak $-\overline{v}$ occurs well inshore of the bar in Run 1 with better agreement with the measurements (Fig. 1e; Secs. 4.1 and 4.2).

The depth-averaged cross-shore PGF decomposition (63) shows that WEC contribution $P^{wec\,x}$ is a significant modification of $P^{tot\,x}$, although shallow breaking (Runs 1 or 2) has a larger $P^{wec\,x}$ than deep breaking (Fig. 13). $P^{tot\,x}$ for Run 3 is primarily led by $P^{c\,x}$ and the quasi-static P^{qsx}, corresponding to the classical barotropic cross-shore momentum balance (*cf.,* Bowen et al., 1968; Uchiyama et al., 2009). For Runs 1 and 2, $P^{wec\,x}$ is dominated by $P^{bh\,x}$ and $P^{qs\,x}$; *i.e.*, $P^{tot\,x}$ is modified significantly by the vertical current shear through $P^{bh\,x}$. This mechanism causes the difference in the wave-induced sea-level rise (setup) between the 2D and 3D cases in Fig. 1c. The WEC surface pressure boundary correction $P^{pc\,x}$ is small for all cases here.

Leading terms in the 3D cross-shore momentum balance for both Runs 1 and 3 (Fig. 14a-e - 15a-e) show the central role of vertical mixing D^{wx} in the bar and shore regions. It vertically connects the surface-intensified breaking to the bottom drag in the cross-shore force balance (in combination with a nearly barotropic PGF). The increase of $D^{wx} < 0$ with height and the bottom-intensified structure of cross-shore advection and VF induce the u recirculation in Fig. 2a; however, the features are much weaker with deep breaking (Run 3), as is the recirculation itself (Fig. 4b).

The WEC role in the alongshore momentum balance (Fig. 14f-h) is even more striking because VF has a significant decrease with depth in balancing the baroclinic distributions of both advection and vertical mixing (whereas VF merely balances advection in the depth-averaged budget; Fig. 12). With

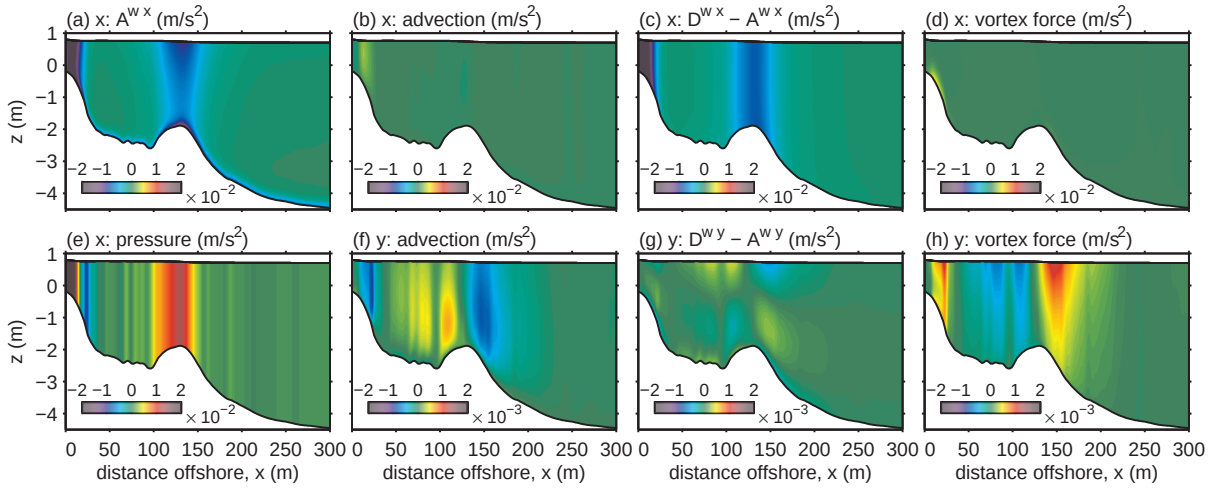

Figure 15: Same as Fig. 14, but for Run 3

shallow breaking (Run 1), advection and vertical mixing primarily redistribute v vertically, while VF is mainly a horizontal redistribution. Even with deep breaking (Run 3), VF has significant vertical variation (Fig. 15h). This implies that in shallow littoral regions like DUCK94, it is necessary to have a fully 3D structure for Stokes drift and VF, unlike in the NA07 model. The primary alongshore momentum balance occurs between advection and vertical mixing in Run 1, particularly over the bar and near the shoreward boundary, where the recirculating u is most prominent, and VF enters at the same order of magnitude. In Run 3 VF contributes relatively more to balance the advection, while the vertical mixing plays a secondary role (Fig. 15f-h). The alongshore non-conservative forcing A^{wy} (not shown) is proportional to A^{wx} by definition, hence always negative to drive the negative v.

In summary, WEC is quantitatively important for $\mathbf{u}(x,z)$ in the surf zone momentum balance through both VF and especially $\mathbf{P}^{wec}$. A similar conclusion is in NA07 regarding VF, although its vertical structure is neglected there.

5. Model Comparisons for a Plane Beach

Another test case is a littoral flow driven by obliquely incident waves on a plane beach with a uniform slope of 1:80. This problem was posed in HW09 to comparatively assess a quasi-3D model (SHORECIRC) and a fully-3D model (developed in W08 using ROMS), both based upon a radiation-stress formalism. The W08 model is based on a set of wave-averaged equations derived by Mellor (2003, 2005) using a GLM-like vertical mapping approach with a depth-varying radiation stresses. Here we compare the latter solution with ones using the present ROMS model with identical wave fields obtained using SWAN without CEW. As described in HW09, the offshore spectral waves are specified by the JONSWAP spectrum for 2 m significant wave height H_{sig} with a peak period of 10 s at an angle of 10 degrees off the shore-normal direction. A quasi-barotropic quadratic bottom drag model is used:

$$\boldsymbol{\tau}^{cd}_{bot} = \rho_0 c_D |\overline{\mathbf{u}}| \mathbf{u}\,, \tag{64}$$

with $c_D = 0.0015$. For 3D runs $\mathbf{u}$ in (64) is the horizontal velocity at the bottom-most grid cells, whereas it is $\overline{\mathbf{u}}$ in a 2D barotropic run. There are minor functional differences between the two models — the W08 model has a wetting/drying capability (whereas our model imposes a solid wall boundary with the minimum water depth, $h_{min} = 0.01$ m, at the shoreward boundary), and it relies on a GLS $k-\epsilon$ turbulence

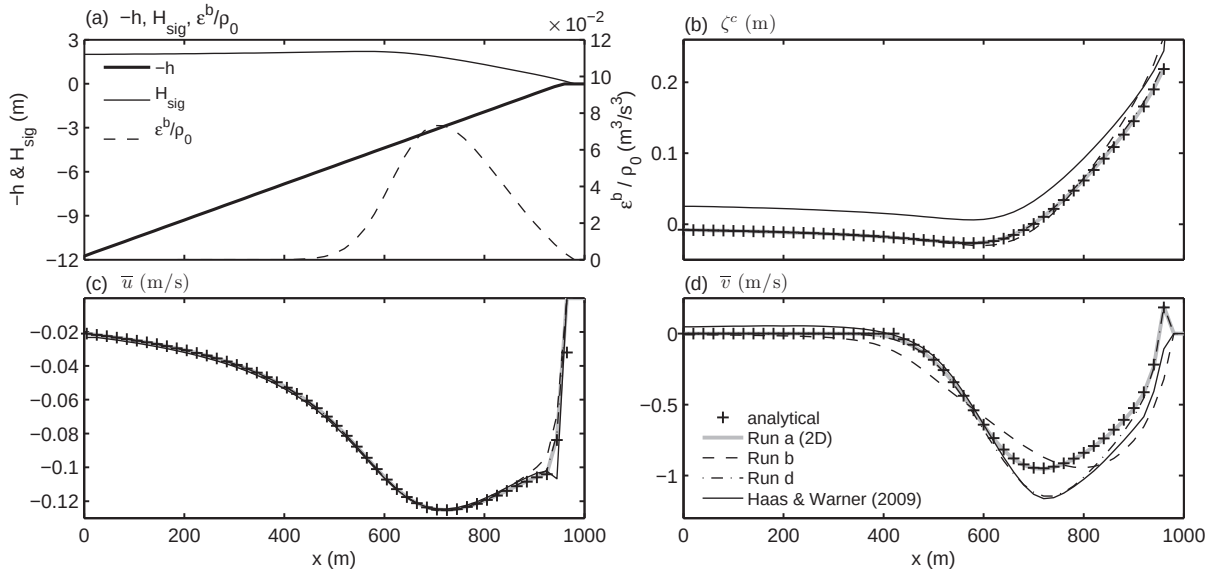

Figure 16: Plane-beach cross-shore profiles of (a) depth h, significant wave height H_{sig}, and breaking dissipation rate ϵ^b/ρ_0; (b) ζ^c; (c) $\overline{u}$; and (d) $\overline{v}$. Runs a, b, and d are compared with the HW09 solution. Plus marks depict the analytical solution (66)-(68).

closure model (Warner et al., 2005) (whereas our model uses either the modified KPP or the analytical model in (65); however, these do not dominate the solution differences we present).

The horizontal extent of the domain is 1180 m in x (cross-shore) × 140 m in y (alongshore) with grid spacings of $\Delta x = \Delta y = 20$ m. The model coordinates have a west-coast orientation, with the offshore open boundary located at $x = 0$. The resting depth h varies from 12 m to 0.01 m (h_{min}), and is discretized with 20 uniform vertical s levels. Boundary conditions are alongshore periodicity, zero normal flux and tangential Neumann conditions at the shoreline boundary, and Chapman-type radiation with weak nudging for $\overline{u}$ and ζ^c (as in Sec. 4) at the offshore boundary. Rotation is excluded with $f = 0$. There is no lateral momentum diffusion, stratification, nor surface wind/heat/freshwater fluxes. Roller waves and bottom streaming are excluded. We conduct four simulations with the present model: a 2D barotropic case (Run a), and three 3D cases with breaking acceleration $\mathbf{B}^b$ (48) using a type III shape function (53) with either $k_b = (0.2H_*)^{-1}$ (Run b), $k_b = 2k$ (Run c), or the same as Run c but with a parabolic profile for vertical mixing (Run d). The last run mimics the eddy viscosity (K_v) distribution in the W08 model, *viz.*,

$$K_v(z) = 0.011\,(h+z)\left[1.0 - \frac{h+z}{D}\right]. \tag{65}$$

In our modified KPP, we use a type II shape function with $k_{Kv} = (1.2H_*)^{-1}$ and $c_b = 0.03$ for Runs b and c. For each run the time integration is continued until a steady solution occurs.

5.1. Barotropic Fields

Uchiyama et al. (2009) show for steady, alongshore-uniform, unstratified, non-rotating solutions that the barotropic continuity balance can be integrated in x from the shoreline to yield the offshore-directed, anti-Stokes cross-shore transport velocity,

$$\overline{u} = -\overline{u^{St}}\,. \tag{66}$$

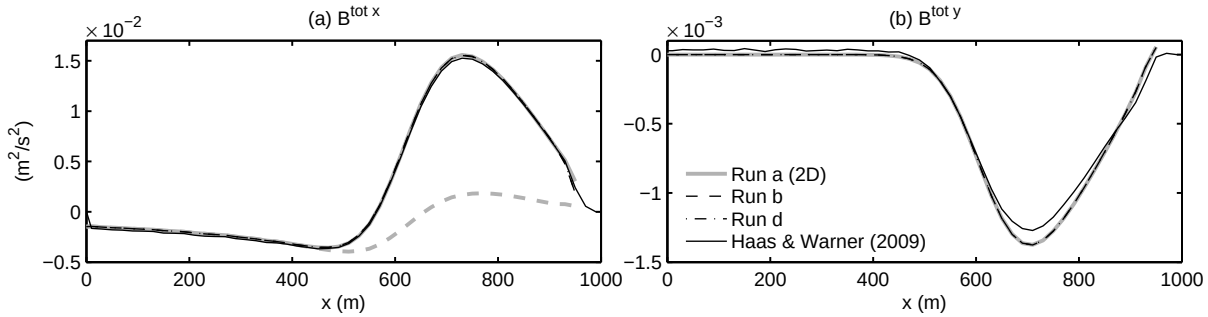

Figure 17: Plane-beach profiles of (a) cross-shore and (b) alongshore components of $\mathbf{B}^{tot}$ for all four runs. In addition, the gray dashed line in (a) is the quasi-static PGF, $-gD\partial_x\hat{\zeta}$, for Run a.

An analytical solution for the $\overline{v}$ is obtained from the mean alongshore momentum balance, where (66) implies separate sub-balances between the VF and alongshore advection (*i.e.,* $\overline{u}\,\partial_x\,\overline{v} = -\overline{u^{St}}\,(\hat{\mathbf{z}}\cdot\nabla_\perp\times\overline{\mathbf{u}})$) and between bottom drag and breaking acceleration:

$$\rho_0 c_D|\overline{\mathbf{u}}|\overline{v} = \frac{\epsilon^b k_y}{\sigma}\,, \tag{67}$$

where $|\overline{\mathbf{u}}| = \sqrt{\overline{u}^2+\overline{v}^2}$. The cross-shore barotropic momentum balance is dominated by PGF and breaking acceleration:

$$g\partial_x\left(\zeta^c-\hat{\zeta}\right) \approx \frac{\epsilon^b k_x}{\rho_0 D\sigma}\,. \tag{68}$$

By integrating (68) from the offshore boundary with $\zeta^c\,|_{x=0} = \hat{\zeta}$ (assuming $\epsilon^b\,|_{x=0} = 0$), the $\zeta^c(x)$ profile is approximately retrieved (*e.g.,* Longuet-Higgins and Stewart, 1962; Bowen et al., 1968). With (66) - (68) and (7) plus the SWAN-produced wave data for ϵ^b, $\mathbf{k}$, and $\mathcal{A}$, we can readily calculate analytical solutions for $\overline{\mathbf{u}}(x)$ and $\zeta^c(x)$.

The shoreward decrease in H_{sig} occurs because of ϵ^b, while refractive wave shoaling has a weak influence (Fig. 16a). Wave breaking occurs around $500 < x < 1000$ m with the peak near $x = 700$ m. The ROMS ζ^c in Fig. 16b generally agrees well with the analytical ζ^c from (68). A minor deviation arises in the case with a shallow breaking force (Run b) near the shoreline by Bernoulli head effect (as in Sec. 4.8). A slightly larger deviation in ζ^c is also found with the W08 model; because it extends far offshore, we suspect it is an artifact from the ocean boundary condition, but it causes only a modest discrepancy compared to the 3D differences emphasized in Sec. 5.2. $\overline{u}$ in Fig. 16c is in almost perfect agreement with (66) for all the cases. $\overline{v}$ also corresponds to the analytical solution (67) fairly well, particularly for Run a (2D) (Fig. 16d) while the 3D cases show deviations because of the 3D current in the bottom drag force. $\overline{v}$ peaks at almost the same cross-shore location for all the cases, except for Run b with a more onshore $|\overline{v}|$ maximum because of a cross-shore momentum imbalance associated with the $\mathbf{A}^w$ and vertical mixing $\mathbf{D}^w$ (47), consistent with DUCK94 results (Secs. 4.4 and 4.8). In the breaking zone in Run d, $\overline{v}$ coincides with that for the W08 model. The W08 model produces a small positive $\overline{v}$ opposing the incident wave direction in the offshore ($x < 500$ m). Run c has a sufficiently similar answer to Run d that we do not show it here, indicating an insensitivity to the particular $K_v(z)$. All the cases shown here generally agree well with the analytical depth-averaged solutions, although HW09 has a slightly larger mismatch and a non-zero value offshore (in the direction opposite to the incident waves), again probably a boundary condition artifact.

In the present model the vertically-integrated WEC accelerations by breaking and and the quasi-static PGF may be combined as

$$\mathbf{B}^{tot} = \int_{-h}^{\zeta^c} \mathbf{B}^b dz + gD\nabla_\perp \hat{\zeta}\,. \tag{69}$$

In W08 the 3D horizontal radiation-stress divergence $\mathbf{S}$ is

$$\mathbf{S} = (S^x, S^y) = \left(-\frac{\partial S_{xx}}{\partial x} - \frac{\partial S_{yx}}{\partial y} + \frac{\partial S_{px}}{\partial z}\,,\; -\frac{\partial S_{xy}}{\partial x} - \frac{\partial S_{yy}}{\partial y} + \frac{\partial S_{py}}{\partial z} \right) \tag{70}$$

(Mellor, 2003; Warner et al., 2008), with an associated $\mathbf{B}^{tot} = \int_{-h}^{\zeta^c} \mathbf{S}\, dz$. Figure 17 shows that the $B^{tot\,x}$ profiles are essentially identical between the two models and unchanged among our different cases. There is some small difference in $B^{tot\,y}(x)$ (Fig. 17b), where the HW09 profile has a slight positive bias associated with the artificial positive $\bar{v}$ in the offshore region ($x < 500$ m; Fig. 16d).

5.2. Vertical Shear

In the surf zone the shallow breaking case (Run b) has the strongest recirculation in $u(x,z)$, with near-surface onshore flow and near-bed offshore undertow (Fig. 18). This pattern is similar to that in the DUCK94 breaking regions (Fig. 4). The other 3D cases (Run d and HW09) induce much weaker recirculation in association with deeper breaker acceleration profiles. In contrast, Run b has the weakest $v(x,z)$, while Run d and HW09 have similar v. The modified KPP scheme concentrates $K_v(x,z)$ near the surface in the breaking zone (Run b), while the other cases have a mid-depth maximum for K_v that increases with depth offshore (Fig. 18: lower-middle). Because Runs b and c (not shown) are more similar in u and v than either is with Run d and HW09, we conclude that the most important distinction is the vertical structure of $\mathbf{B}$, with K_v providing a lesser distinction (*cf.*, Sec. 4.5). All models yield the same anti-Stokes $\bar{u}(x)$ (Fig. 16), but the W08 model generates an onshore surface $u(x,z)$ even in the offshore region outside the breaking zone, which is not seen with the present model. (HW09 shows that the SHORECIRC model also yields a less sheared u profile in the offshore region than the W08 model.)

In the W08 model the radiation stress tensor (70), *e.g.*, S_{xy}, can be rearranged as

$$S_{xy} = \frac{E}{\rho_0}\frac{k_x k_y}{k}\frac{\cosh 2k(h+z)+1}{\sinh 2kD}\,. \tag{71}$$

This 3D radiation stress has a depth-dependency of $\cosh[2k(h+z)]$ function, consistent with our type III vertical shape function $f^b(z)$ for $\mathbf{B}^b$ with $k_b = 2k$ in (53). This becomes nearly constant in shallow water ($kh \to 0$), including over much of the surf zone. Thus, $\mathbf{S}$ in the W08 is vertically homogeneous (Fig. 18: bottom panels), in contrast to the shallow $\mathbf{B}^b$ in Run b. In Run d, $\mathbf{B}^b$ resembles $\mathbf{S}$. Therefore Runs b and d (and HW09) are closely related to Runs 1 and 3 in the DUCK experiment (Sec. 4, Fig. 5) in terms of the depth-dependency parameter choice. Accordingly, it is anticipated that the 3D radiation-stress model (*e.g.*, Mellor, 2003) could have noticeable deficiency for surfzone applications. In addition, a more vertically-sheared velocity field with the appropriate $\mathbf{B}^b$ forcing is essential to more correct VF representation that leads to significant modification in the momentum balance as seen in Sec. 4.8, particularly through the horizontal and vertical VF and the Bernoulli-head pressure force $\mathcal{K}$. The radiation-stress divergence contains multiple aspects of WEC: the conservative VF (if the accompanying wave model takes CEW into account appropriately; Lane et al., 2007), the conservative gradient of the quasi-static PGF $g\nabla_\perp\hat{\zeta}$ (as part of S_{xx} and S_{yy}; *e.g.*, Longuet-Higgins and Stewart, 1964), and the non-conservative acceleration $\mathbf{B}^b$. When $\mathbf{S}$ is evaluated with the vertical structure of the leading-order primary wave solution (*e.g.*, Mellor, 2003), then it causes an underestimation of vertical shear in u. The

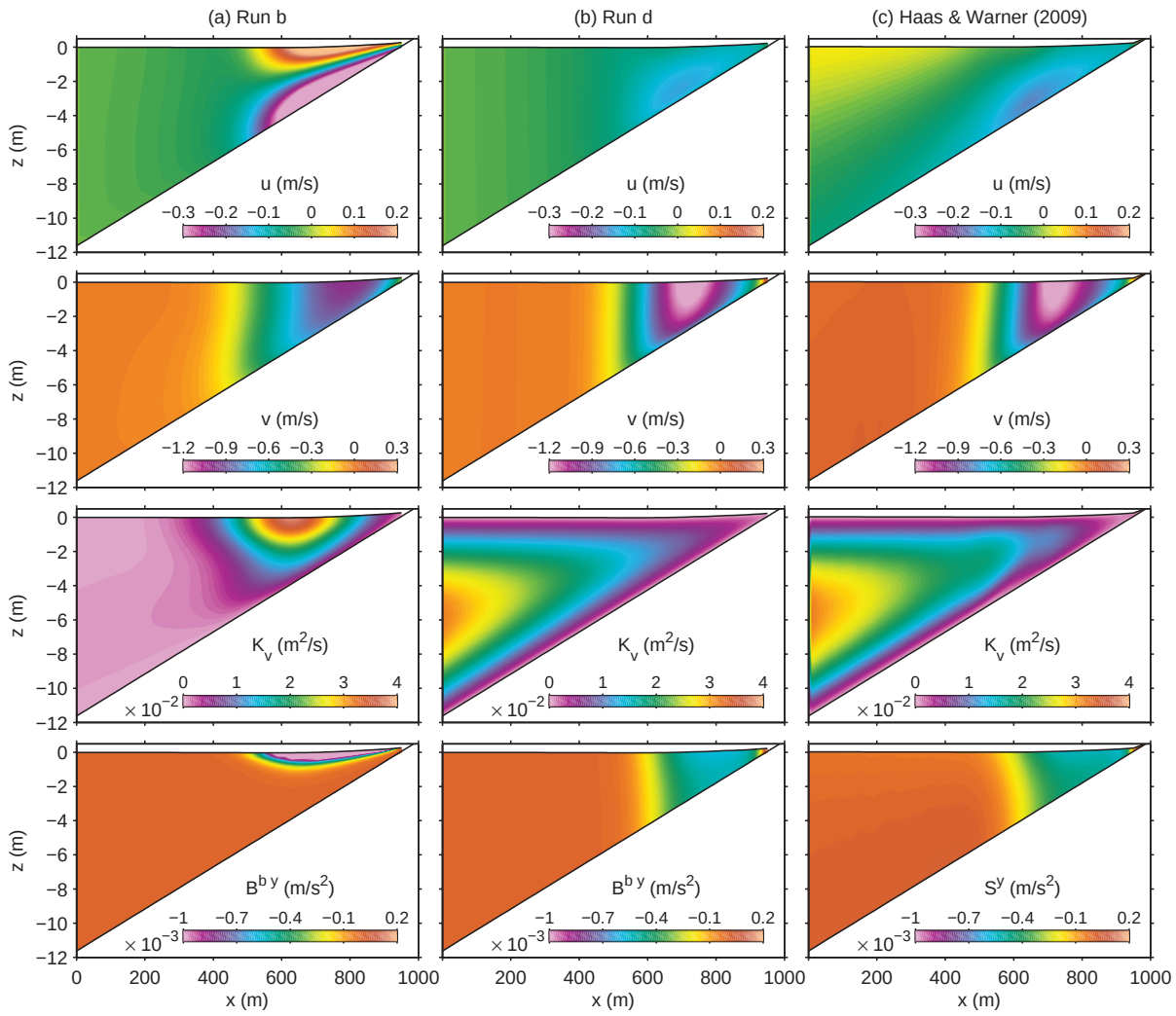

Figure 18: Model comparisons among Runs b and d for the present model and the W08 model (in HW09): (top) u; (upper-middle) v; (lower-middle) K_v; and (bottom) $\mathbf{B}^b$ (Runs b and d) or $\mathbf{S}$ (HW09).

present model cleanly separates the different WEC influences and allows them to have different spatial distributions.

6. Summary and Prospects

Wave-current interaction with a vortex-force (VF) formalism is implemented in a fully-3D oceanic circulation model (ROMS) intended for use in a wide range of conditions. The Eulerian wave-averaged, multi-scale asymptotic theory by MRL04 is adapted to be appropriate for ROMS. Conservative wave effects include the VF, the Stokes-Coriolis force, Bernoulli head, and quasi-static pressure and sea-level responses. Non-conservative accelerations are included through parameterizations of depth-induced breaking, associated surface rollers, and wave-induced streaming dissipation at the bottom. Wave-enhanced mixing from surface breakers is included (adapted from Battjes, 1975), as is wave-enhanced bottom stress and bottom-boundary layer mixing in a KPP parameterization (Large et al., 1994). Here the model is applied to the surf zone off Duck, NC and demonstrates a good agreement with *in situ* velocity data

for appropriate choices of several model parameters. The model is further compared to another ROMS-based 3D model with a depth-dependent radiation-stress formalism (Warner et al., 2008) for a littoral current on a gently-sloping plane beach.

Littoral currents are caused by depth-induced wave breaking in the problems solved here. In the DUCK94 problem, alongshore $\overline{v}(x)$ is largest near the topographic bar and has a momentum balance of breaking acceleration against deceleration by bottom drag and vortex force, while cross-shore $\overline{u}(x)$ is an offshore, anti-Stokes transport locally enhanced near the bar and shoreline by breaking and shifted shoreward by VF. Surface-intensified breaking (on a scale $< H_*$) by the primary and roller waves $\mathbf{B}^b$ is essential to reproduce the measured current profiles. $v(x,z)$ peaks shoreward of the bar and has a modest degree of vertical shear, while $u(x,z)$ has two strong recirculations (onshore at surface, offshore at depth) near the bar and shoreline. Wave effects of $\mathbf{B}^b$, vertical mixing, PGF, and vortex force all contribute to the maintenance of the current profiles. Offshore of the breaking region, the wave-induced bottom streaming stress shifts the maximum of the anti-Stokes $u(z) > 0$ upward to mid-depth. Similar conclusions obtain in the plane beach problem, where in particular a previously proposed deep radiation-stress representation greatly underestimates the recirculation in $u(x,z)$ compared to WEC with shallow $\mathbf{B}^b$, K_v^b, and vortex force.

The two applications presented here are of limited generality due to the weakness of the effect of currents on the waves (CEW), the absence of strong alongshore variation (*e.g.,* rip currents), density stratification, interaction with eddying currents, suspended sediments, and even non-hydrostatic current dynamics. We anticipate that significant additional wave-current interaction phenomena will be abundant in these variously more general regimes.

Acknowledgments. We thank John Warner for his comments and for sharing the model data used in Sec. 5. Thanks are due to those who carried out the DUCK94 field experiments and provided online data access. We thank members of the NOPP-CSTMS project and three anonymous reviewers for their constructive suggestions. This work is financially supported by the National Science Foundation (DMS-0723757) and Office of Naval Research (N00014-04-1-0166, N00014-06-1-0945, N00014-08-1-0597).

References

Andrews, D. G., McIntyre, M. E., 1978a. An exact theory of nonlinear waves on a Lagrangian-mean flow. J. Fluid Mech. 89, 609–646.

Andrews, D. G., McIntyre, M. E., 1978b. On wave action and its relatives. J. Fluid Mech. 89, 647–664.

Apotsos, A., Raubenheimer, B., Elgar, S., Guza, R. T., Smith, J. A., 2007. Effects of wave rollers and bottom stress on wave setup. J. Geophys. Res. 112, C02003, doi:10.1029/2006JC003549.

Ardhuin, F., Jenkins, A. D., Belibassakis, K. A., 2008a. Comments on "The three-dimensional current and surface wave equations". J. Phys. Oceanogr. 38, 1340–1350.

Ardhuin, F., Rascle, N., Belibassakis, K. A., 2008b. Explicit wave-averaged primitive equations using a Generalized Lagrangian Mean. Ocean Modelling 20, 35–60.

Battjes, J. A., 1975. Modeling of turbulence in the surfzone. In: Proc. of Symposium on Modeling Techniques 1975 San Francisco, CA. American Society of Civil Engineers, New York, pp. 1050–1063.

Blaas, M., Dong, C., Marchesiello, P., McWilliams, J., Stolzenbach, K., 2007. Sediment transport modeling on Southern Californian shelves: A ROMS case study. Contin. Shelf Res. 27, 832–853.

Blumberg, A. F., Mellor, G. L., 1987. A description of a three-dimensional coastal ocean circulation model. In: Three-Dimensional Coastal Ocean Models. American Grophys. Union, pp. 1 – 16.

Booij, N., Ris, R. C., Holthuijsen, L. H., 1999. A third generation wave model for coastal regions 1. Model description and validation. J. Geophys. Res. 104 C4, 7649–7666.

Bowen, A. J., Inman, D. L., Simmons, V. P., 1968. Wave 'set-down' and wave setup. J. Geophys. Res. 73, 2569–2577.

Burchard, H., 2001. Simulating the wave-enhanced layer under breaking surface waves with two-equation turbulence models. J. Phys. Oceanogr. 31, 3133–3145.

Chen, Q., Dalrymple, R. A., Kirby, J. T., Kennedy, A. B., Haller, M. C., 1999. Boussinesq modeling of a rip current system. J. Geophys. Res. 104, 20,617–20,637.

Church, J. C., Thornton, E. B., 1993. Effects of breaking wave induced turbulence within a longshore current model. Coastal Engineering 20, 1–28.
Craig, P. D., Banner, M. L., 1994. Modeling wave-enhanced turbulence in the ocean surface layer. J. Phys. Oceanogr. 24, 2546–2559.
Craik, A. D. D., Leibovich, S., 1976. A rational model for Langmuir circulations. J. Fluid Mech. 73, 401–426.
Davies, A. G., Villaret, C., 1999. Eulerian drift induced by progressive waves above rippled and very rough beds. J. Geophys. Res. 104 C1, 1465–1488.
Dingemans, M. W., Radder, A. C., Vriend, H. J. D., 1987. Computation of the driving forces of wave-induced currents. Coastal Eng. 11, 539–563.
Durski, S. M., Glenn, S. M., Haidvogel, D., 2004. Vertical mixing schemes in the coastal ocean: Comparision of the level 2.5 Mellor-Yamada scheme with an enhanced version of the K profile parameterization. J. Geophys. Res. 109, C01015, doi:10.1029/2002JC001702.
Elgar, S., Guza, R. T., Raubenheimer, B., Herbers, T. H. C., Gallagher, E. L., 1998. Spectral evolution of shoaling and breaking waves on a barred beach. J. Geophys. Res. 103, 15,797–15,805.
Feddersen, F., Guza, R. T., Elgar, S., Herbers, T. H. C., 1998. Alongshore momentum balances in the nearshore. J. Geophys. Res. 103, 15,667–15,676.
Fredsøe, J., Deigaard, R., 1995. Mechanics of Coastal Sediment Transport. World Scientific, Singapore.
Gallagher, E. L., Boyd, W., Elgar, S., Guza, R. T., Woodward, B., 1996. Perfomance of a sonar altimeter in the nearshore. Mar. Geol. 133, 241–248.
Gallagher, E. L., Elgar, S., Guza, R. T., 1998. Observations of sand bar evolution on a natural beach. J. Geophys. Res. 103, 3203–3215.
Galperin, B., Kantha, L. H., Hassid, S., Rossati, A., 1988. A quais-equilibrium turbulent energy model for geophysical flows. J. Atmos. Sci. 45, 55–62.
Garcez Faria, A. F., Thornton, E. B., Lippmann, T. C., Stanton, T. P., 2000. Undertow over a barred beach. J. Geophys. Res. 105, 16,999–17,010.
Garcez Faria, A. F., Thornton, E. B., Stanton, T. P., Soares, C. V., Lippmann, T. C., 1998. Vertical profiles of longshore currents and related bed stress and bottom roughness. J. Geophys. Res. 103, 15,667–15,676.
Garrett, C., 1976. Generation of Langmuir circulations by surface waves—a feedback mechanism. J. Mar. Res. 34, 116–130.
Groeneweg, J., 1999. Wave-current interaction in a generalized Lagrangian mean formulation. PhD thesis, Delft University of Technology, Delft, The Netherland.
Haas, K. A., Warner, J. C., 2009. Comparing a quasi-3D to a full 3D nearshore circulation model: SHORECIRC and ROMS. Ocean Modeling 26, 91–103.
Hasselmann, K., 1971. On the mass and momentum transfer between short gravity waves and larger-scale motions. J. Fluid Mech. 50, 189–201.
Jones, N. L., Monismith, S. G., 2008. Modeling the influence of wave-enhanced turbulence in a shallow tide- and wind-driven water column. J. Geophys. Res. 113, C03009, doi:10.1029/2007JC004246.
Kanarska, Y., Shchepetkin, A. F., McWilliams, J. C., 2007. Algorithm for non-hydrostatic dynamics in the Regional Oceanic Modeling System. Ocean Modelling 18, 143–174.
Klopman, G., 1994. Stokes transport. WL-Delft Hydraulics Report H840.30, Part II.
Lane, E. M., Restrepo, J. M., McWilliams, J. C., 2007. Wave-current interaction: A comparison of radiation-stress and vortex-force representations. J. Phys. Oceanogr. 37, 1122–1141.
Large, W. G., McWilliams, J. C., Doney, S. C., 1994. Oceanic vertical mixing: A review and a model with nonlocal boundary layer parameterisation. Rev. Geophys. 32, 363–403.
Leibovich, S., 1980. On wave-current interaction theories of Langmuir circulations. J. Fluid Mech. 99, 715–724.
Lentz, S. J., Fewings, M., Howd, P., Fredericks, J., Hathaway, K., 2008. Observations and a model of undertow over the inner continental shelf. J. Phys. Oceanogr. 38, 2341–2357.
Lesser, G. R., Roelvink, J. A., van Kester, J. A. T. M., Stelling, G. S., 2004. Development and validation of a three-dimensional morphological model. Coastal Engineering 51, 883–915.
Lewis, J. K., 1997. A three-dimensional ocean circulation model with wave effects. In: Spaulding, M. L., Blumberg, A. F. (Eds.), Proc. of the 5th International Conference on Estuarine and Coastal Modeling, Alexandria, VA. American Society of Civil Engineers, Reston, VA, pp. 584–600.
Long, C. E., 1996. Index and bulk parameters for frequency-direction spectra measured at CERC Field Research Facility, June 1994 to August 1995. U.S. Army Corps of Engineers Waterway Experiment Station, Vicksburg, MI, U.S.A.
Longuet-Higgins, M. S., 1953. Mass transport in water waves. Philos. Trans. R. Soc. London, Ser. A 245, 535–581.
Longuet-Higgins, M. S., 1958. The mechanics of the boundary later near the bottom in a progressive wave. Appendix to “An experimental investigation of drift profiles ub a closed channel” by R. C. H Russel and J. D. C. Osorio. In: Proc. of the 6th Coastal Engineering International Conference 1957, Florida. American Society of Civil Engineers, New York, pp. 184–193.
Longuet-Higgins, M. S., 1970. Longshore currents generated by obliquely incident sea waves, 1 & 2. J. Geophys. Res. 75 (33), 6778–6801.

Longuet-Higgins, M. S., 1973. The mechanics of the surfzone. In: Becker, E., Mikhailov, G. K. (Eds.), Proc. of the 13th International Congress of Theoretical and Applied Mathematics 1972, Moscow, USSR. Springer-Verlag, Berlin, pp. 213–228.

Longuet-Higgins, M. S., Stewart, R. W., 1962. Radiation stress and mass transport in gravity waves, with application to 'surf beats'. J. Fluid Mech. 13, 481–504.

Longuet-Higgins, M. S., Stewart, R. W., 1964. Radiation stresses in water waves: a physical discussion, with applications. Deep-Sea Res. 11, 529–562.

McWilliams, J. C., Restrepo, J. M., 1999. The wave-driven ocean circulation. J. Phys. Oceanogr. 29, 2523–2540.

McWilliams, J. C., Restrepo, J. M., Lane, E. M., 2004. An asymptotic theory for the interaction of waves and currents in coastal waters. J. Fluid Mech. 511, 135–178.

McWilliams, J. C., Sullivan, P. P., Moeng, C.-H., 1997. Langmuir turbulence in the ocean. J. Fluid Mech. 334, 1–30.

Mellor, G. L., 2003. The three-dimensional current and surface wave equations. J. Phys. Oceanogr. 33, 1978–1989.

Mellor, G. L., 2005. Some consequences of the three-dimensional currents and surface wave equations. J. Phys. Oceanogr. 35, 22912298.

Mellor, G. L., 2008. The depth-dependent current and wave interaction equations: A revision. J. Phys. Oceanogr. 38, 25872596.

Mellor, G. L., Yamada, T., 1982. Development of a turbulent closure model for geophysical fluid problems. Rev. Geophys. 20, 851–875.

Nairn, R. B., Roelvink, J. A., Southgate, H. N., 1991. Transition zone width and implications for modelling surfzone hydrodynamics. In: Edge, B. L. (Ed.), Proc. of the 22nd Coastal Engineering International Conference 1990, Delft, The Netherlands. American Society of Civil Engineers, New York, pp. 68–82.

Newberger, P. A., Allen, J. S., 2007a. Forcing a three-dimensional, hydrostatic, primitive-equation model for application in the surf zone: 1. Formulation. J. Geophys. Res. 112, C08018, doi:10.1029/2006JC003472.

Newberger, P. A., Allen, J. S., 2007b. Forcing a three-dimensional, hydrostatic, primitive-equation model for application in the surf zone: 2. Application to DUCK94. J. Geophys. Res. 112, C08019, doi:10.1029/2006JC003474.

Okayasu, A., Shibayama, T., Mimura, N., 1986. Velocity field under plunging waves. In: Edge, B. L. (Ed.), Proc. of the 20th Coastal Engineering International Conference 1986, Taipei, Taiwan. American Society of Civil Engineers, New York, pp. 660–674.

Özkan-Haller, H. T., Kirby, J. T., 1999. Nonlinear evolution of shear instabilities of the longshore current: A comparison of observations and computations. J. Geophys. Res. 104, 25,953–25,984.

Özkan-Haller, H. T., Li, Y., 2003. Effects of wave-current interaction on shear instabilities of longshore currents. J. Geophys. Res. 108, C5, 3139, doi:10.1029/2001JC001287.

Perrie, W., Tang, C. L., Hu, Y., DeTracy, B. M., 2003. The impact of waves on surface currents. J. Phys. Oceanogr. 33, 2126–2140.

Phillips, O. M., 1977. The Dynamics of the Upper Ocean. Cambridge University Press, Cambridge, UK.

Rascle, N., 2007. Impact of waves on the ocean circulation. PhD thesis, Université de Bretagne Occidentale - Brest, Brest, France.

Rascle, N., Ardhuin, F., Terray, E. A., 2006. Drift and mixing under the ocean surface: A coherent one-dimensional description with application to unstratified conditions. J. Geophys. Res. 111, C03016, doi:10.1029/2005JC003004.

Rascle, N., Ardhuin, F., Terray, E. A., 2009. Drift and mixing under the ocean surface revisited: Stratified conditions and model-data comparisons. J. Geophys. Res. 114, C02016, doi:10.1029/2007JC004466.

Raubenheimer, B., Guza, R. T., Elgar, S., 2001. Field observation of wave-driven setdown and setup. J. Geophyis. Res. 106 C3, 4629–4638.

Reniers, A. J. H. M., Roelvink, J. A., Thornton, E. B., 2004a. Morphodynamic modeling of an embayed beach under wave group forcing. J. Geophys. Res. 109, C01030, doi:10.1029/2002JC001586.

Reniers, A. J. H. M., Thornton, E. B., Stanton, T. P., Roelvink, J. A., 2004b. Vertical flow structure during sandy duck: observations and modeling. Coastal Engineering 51, 237–260.

Ruessink, B., Miles, J., Feddersen, F., Guza, R., Elgar, S., 2001. Modeling the alongshore current on barred beach. J. Geophyis. Res. 106 C10, 22,451–22,463.

Shchepetkin, A. F., McWilliams, J. C., 2005. The Regional Oceanic Modeling System: A split-explicit, free-surface, topography-following-coordinate oceanic model. Ocean Modeling 9, 347–404.

Shchepetkin, A. F., McWilliams, J. C., 2008. Computational kernel algorithms for fine-scale, multiprocess, longtime oceanic simulations. In: Temam, R., Tribbia, J. (Eds.), Handbook of Numerical Analysis: Computational Methods for the Ocean and the Atmosphere. Elsevier Science, pp. 119–181.

Shchepetkin, A. F., McWilliams, J. C., 2010. KPP revisited(in preparation).

Shi, F., Kirby, J. T., Haas, K., 2006. Quasi-3D nearshore circulation equations: a CL-vortex force formulation. In: Proc. 30th Int. Conf. Coastal Eng. Amer. Soc. Civil Eng., pp. 1028–1039.

Smith, J., 2006. Wave-current interactions in finite depth. J. Phys. Oceanogr. 36, 1403–1419.

Soulsby, R. L., 1995. Bed shear-stresses due to combined waves and currents. In: Stive, M., Fredsøe, J., Hamm, L., Soulsby, R., Teisson, C., Winterwerp, J. (Eds.), Advances in Coastal Morphodynamics. Delft Hydraulics, Delft, the Netherlands, pp.

4–204–23.
Soulsby, R. L., 1997. Dynamics of marine sands, a manual for practical applications. Thomas Telford, London, UK.
Stive, M. J. F., De Vriend, H. J., 1994. Shear stresses and mean flow in shoaling and breaking waves. In: Edge, B. L. (Ed.), Proc. of the 24th Coastal Engineering International Conference 1994, Kobe, Japan. American Society of Civil Engineers, New York, pp. 594–608.
Sullivan, P. P., McWilliams, J. C., Melville, W. K., 2007. Surface gravity wave effects in the oceanic boundary layer: Large Eeddy Simulation with vortex force and stochastic breakers. J. Fluid Mech. 593, 405–452.
Svendsen, I. A., 1984a. Mass flux and undertow in a surf zone. Coastal Engineering 8, 347–365.
Svendsen, I. A., 1984b. Wave height and set-up in a surf zone. Coastal Engineering 8, 303–329.
Tajima, Y., Madsen, O. S., 2006. Modeling near-shore waves, surface rollers, and undertow velocity profiles. J. Waterway, Port, Coastal, and Ocean Eng. 132, 429–438.
Terray, E. A., Donelan, M. A., Agrawal, Y. C., Drennan, W. M., Kahma, K. K., Williams, A. J., Hwang, P. A., Kitaigorodskii, S. A., 1996. Estimates of kinetic energy dissipation under breaking waves. J. Phys. Oceanogr. 26, 792–807.
Terrile, E., Brocchini, M., Christensen, K. H., Kirby, J. T., 2008. Dispersive effects on wave-current interaction and vorticity transport in nearshore flow. Phys. Fluid 20, 036602, doi:10.1063/1.2888973.
Thornton, E. B., Guza, R. T., 1983. Transformation of wave height distribution. J. Geophys. Res. 88 C10, 5925–5938.
Thornton, E. B., Whitford, D. J., 1990. Longshore currents over a barred beach: Part II, Model. Naval Postgraduate School, Monterey, California, pp. 1–30.
Trowbridge, J., Madsen, O. S., 1984. Turbulent wave boundary layers, 2. Second-order theory and mass transport. J. Geophys. Res. 89 C5, 7999–8007.
Uchiyama, Y., McWilliams, J. C., 2008. Infragravity waves in the deep ocean: Generation, propagation, and seismic hum excitation. J. Geophys. Res. 113, C07029, doi:10.1029/2007JC004562.
Uchiyama, Y., McWilliams, J. C., Restrepo, J. M., 2009. Wave-current interaction in nearshore shear instability analyzed with a vortex-force formalism. J. Geophys. Res. 114, C06021, doi:10.1029/2008JC005135.
Umlauf, L., Burchard, H., Hutter, K., 2003. Extending the $k-\omega$ turbulence model towards oceanic applications. Ocean Modelling 5, 195–218.
Walstra, D. J. R., Roelvink, J. A., Groeneweg, J., 2000. Calculation of wave-driven currents in a 3D mean flow model. In: Edge, B. L. (Ed.), Proc. of the 27th Coastal Engineering International Conference 2000, Sydney, Australia. American Society of Civil Engineers, New York, pp. 1050–1063.
Warner, J. C., Sherwood, C. R., Arango, H. G., Signell, R. P., 2005. Performance of four turbulence closure models implemented using a generic length scale method. Ocean Modeling 8, 81–113.
Warner, J. C., Sherwood, C. R., Signell, R. P., Harris, C. K., Arango, H. G., 2008. Development of a three-dimensional, regional, coupled wave, current, and sediment transport model. Comp. Geosci. 34, 1284–1306.
Xia, H., Xia, Z., Zhu, L., 2004. Vertical variation in radiation stress and wave-induced current. Coastal Engineering 51, 309–321.
Xie, L., Wu, K., Pietrafesa, L. J., Zhang, C., 2001. A numerical study of wave-current interaction through surface and bottom stresses: Wind-driven circulation in the South Atlantic Bight under uniform winds. J. Geophys. Res. 106, C8, 16,841–16,855.
Xu, Z., Bowen, A. J., 1994. Wave- and wind-driven flow in water of finite depth. J. Phys. Oceanogr. 24, 1850–1866.
Yu, J., Slinn, D. N., 2003. Effect of wave-current interaction on rip currents. J. Geophys. Res. 108, C3, 3088–3106.